



## Article

# A Data-Driven Model on Google Earth Engine for Landslide Susceptibility Assessment in the Hengduan Mountains, the Qinghai–Tibetan Plateau

Wenhuan Wu <sup>1,2,3</sup> , Qiang Zhang <sup>1,3,\*</sup> , Vijay P. Singh <sup>4</sup>, Gang Wang <sup>1,3</sup> , Jiaqi Zhao <sup>1,3</sup>, Zexi Shen <sup>1,3</sup> and Shuai Sun <sup>1,3,5</sup>

- <sup>1</sup> State Key Laboratory of Earth Surface Processes and Resource Ecology, Beijing Normal University, Beijing 100875, China
- <sup>2</sup> National Key Laboratory of Remote Sensing Information and Imagery Analyzing Technology, Beijing Research Institute of Uranium Geology, Beijing 100029, China
- <sup>3</sup> Faculty of Geographical Science, Beijing Normal University, Beijing 100875, China
- <sup>4</sup> Department of Biological and Agricultural Engineering, Texas A&M University, College Station, TX 77469, USA
- <sup>5</sup> National Meteorological Information Center, China Meteorological Administration, Beijing 100875, China
- \* Correspondence: zhangq68@bnu.edu.cn; Tel.: +86-10-58807086

**Abstract:** Amplifying landslide hazards in the backdrop of warming climate and intensifying human activities calls for an integrated framework for accurately evaluating landslide susceptibility at fine spatiotemporal resolutions, which is critical for the mitigation of increasingly high landslide disaster risks. Yet, dynamic landslide susceptibility mapping is still lacking. Using high-quality data, from 14,435 landslides and non-landslides, we developed an efficient holistic framework for evaluating landslide susceptibility, considering landslide-relevant internal and external factors based on cloud computing platform and algorithmic models, which enables dynamic updating of a landslide susceptibility map at the regional scale, particularly in regions with highly complicated topographical features such as the Hengduan Mountains, as considered in this study. We compared Classification and Regression Trees (CART), Support Vector Machines (SVM), and Random Forest (RF) classifiers to screen out the best portfolio model for landslide susceptibility mapping on the Google Earth Engine (GEE) platform. We found that the Random Forest (RF) classifier integrated with synergy mode had the best modeling performance, with 90.48% and 89.24% accuracy and precision, respectively. We also found that forests and grasslands had the controlling effect on the occurrence of landslides, while human activities had a notable inducing effect on the occurrence of landslides within the Hengduan Mountains. This study highlights the performance of the holistic landslide susceptibility evaluation framework proposed in this study and provides a viable technique for landslide susceptibility evaluation in other regions of the globe.

**Keywords:** landslide susceptibility assessment; synergy mode; random forest; google earth engine; Hengduan Mountains



**Citation:** Wu, W.; Zhang, Q.; Singh, V.P.; Wang, G.; Zhao, J.; Shen, Z.; Sun, S. A Data-Driven Model on Google Earth Engine for Landslide Susceptibility Assessment in the Hengduan Mountains, the Qinghai–Tibetan Plateau. *Remote Sens.* **2022**, *14*, 4662. <https://doi.org/10.3390/rs14184662>

Academic Editor: Michele Saroli

Received: 14 July 2022

Accepted: 13 September 2022

Published: 19 September 2022

**Publisher's Note:** MDPI stays neutral with regard to jurisdictional claims in published maps and institutional affiliations.



**Copyright:** © 2022 by the authors. Licensee MDPI, Basel, Switzerland. This article is an open access article distributed under the terms and conditions of the Creative Commons Attribution (CC BY) license (<https://creativecommons.org/licenses/by/4.0/>).

## 1. Introduction

A landslide is a natural disaster that may cause thousands of fatalities and inflict massive damage on infrastructure [1–3]. With the projected increase in extreme precipitation [4], land resources dwindling, and urban development spiraling, landslides are increasing in frequency, scope, and destructive capacity [5]. The International Disaster Database (EM-DAT) shows that between 2000 and 2020, landslides accounted for 4.51% of all natural disasters, while 13.05% of these landslide disasters occurred in China [6]. The actual landslide disasters and their risk may be higher than recorded in EM-DAT landslide catalogs, since many landslides go unreported [7,8]. Landslide susceptibility is

the likelihood of a landslide occurring in an area, depending on local topographical and environmental variables [9]. It predicts “where” landslides are likely to occur [10]. Landslide susceptibility (LS) mapping is the first step in landslide disaster reduction plans [11,12].

Reliable LS evaluation greatly depends on the quality and availability of data and a proper modeling framework [13–15]. Studies of a LS evaluation model can be classified as qualitative or quantitative [16]. Qualitative methods are based on an expert’s prior knowledge, including geomorphological analysis, heuristic approach, specific user indicators, and variable mapping methods [14,17], whereas quantitative methods include statistical methods such as binary statistical analysis, Logistic Regression, and Discriminant Analysis [18–21] and machine learning methods such as Fuzzy Logic, Artificial Neural Network, Support Vector Machines, Naive Bayes, Decision Tree, Random Forest [22–27]; and Deep Learning methods [28]. However, when compared with traditional machine learning methods, Deep Learning methods perform similarly well in terms of prediction accuracy and evaluation of LS [29]. The quality of a LS map produced by a model relies heavily on the accuracy, scale, and number of landslide-related factors considered [13,30,31]. The occurrence and distribution of landslides are closely related to landslide-relevant hazard-causing factors and a hazard-pregnant environment, such as topography, tectonic activity, rock and/or soil types, hydrometeorological setting, land use, and land cover, and anthropogenic activities such as construction, improper drainage, and deforestation [32–35]. Any of these abovementioned factors will cause the instability of mountain slopes and will trigger landslide disasters [36,37]. In addition, a range of index systems were developed for the assessment of LS [13,38]. Spatial geographical information techniques and satellite remote sensing data have greatly improved the assessment of LS at regional to global scales [39–42]. Previous studies used optical imagery [28,43,44] and synthetic aperture radar (SAR) data [45–48] to map the landslide distribution and/or to extract landslide-related information such as soil moisture, land use, road construction, and urban buildings. Satellite-based meteorological data have been widely used for the analysis and evaluation of relationship between precipitation and landslides [49–51]. Geomorphological factors (e.g., elevation, slope, aspect, and curvature) obtained through DEM data, which can be generated from various sources such as radar interferometry (SRTM) and optical stereo images (ASTER DEM) [52], were used to delve into landslide hazards [53]. Current satellite data may provide useful and accurate information about the characteristics and dynamic processes of the earth’s surface involved in the occurrence of landslides. Numerous studies used road net, anastomosis, fault, and seismic vector data, etc., which can be obtained from Open Street Map (OSP) or other open data platforms to assess landslide susceptibility [54–56]. However, taking these driving factors into account and considering an appropriate LS model are challenging and computing-resources-consuming work. With the emergence of Google Earth Engine (GEE), there are abundant data resources and functions, which enable investigations at the regional and global scales [57,58]. Therefore, it is desirable to develop a holistic LS evaluation framework based on a cloud computing platform, machine learning techniques, and multisource data/big data to assess and map landslide susceptibility at the regional and even global scales.

Investigations have highlighted that the high LS areas, spread mainly over Southwest China, i.e., the Hengduan Mountains, are characterized by landslide-prone sedimentary rocks, high seismicity, frequent severe rainfall events, and intensifying human activities [15,59]. The Hengduan Mountains region is dominated by complicated and unique topographical features, complex hydrometeorological conditions, active tectonic movements, and intensifying human activities and is characterized by considerably large differences in elevation, with the largest difference reaching >7300 m above sea level. All these factors help develop an extremely complicated landslide hazard-pregnant environment. Therefore, it is a challenge to identify and map the LS across the Hengduan Mountains region. However, few studies have addressed LS mapping by combining static and dynamic explanatory factors and, hence, cannot delve into the causes behind the proximity of the regions with occurrence of landslides from a holistic viewpoint. In addition, this is needed for the

mitigation of potential landslide hazards at the regional scale, especially in the Hengduan Mountains [60,61]. It should be noted that LS mapping is a challenging task, particularly for regions with complicated topographical features, since the driving factors triggering landslides are complicated, so an efficient assessment framework is needed. To develop a holistic LS evaluation framework based on GEE is a critical first step for the dynamic update of LS map and is also of practical significance for regional mitigation of landslide disasters in a warming climate. Therefore, development of an efficient LS evaluation framework combining static and dynamic explanatory factors, based on multisource datasets and cloud computing platform and machine learning algorithms, is urgently needed. This point constitutes the major motivation of this study.

Here, we present a synergy of static and dynamic explanatory variables based on GEE to evaluate LS at the regional scale and propose a holistic LS evaluation framework. The major objectives of this study, therefore, are to (1) evaluate the influence of the types of landslide-related factors (static, dynamic and both) on LS, (2) elucidate the controlling factors of LS across the Hengduan Mountains region, and (3) propose and develop an efficient and near-real-time LS evaluation framework at the regional scale. This study highlights an efficient LS evaluation framework and helps provide a technique framework for the mapping of LS in other regions of the globe.

## 2. Study Region

The Hengduan Mountains region is located in the southeastern part of the Qinghai–Tibetan Plateau and is a general term for the north–south-oriented parallel mountains in the western part of Sichuan and Yunnan provinces and the eastern part of the Tibet Autonomous Region, covering an area of more than 700,000 km<sup>2</sup>, with elevation ranging from 124 m to 7473 m (Figure 1). Actually, the Hengduan Mountains region is a complete geomorphological partition, in which different subregions have similarities in geomorphological forms, tectonic features, and geomorphological development processes [62]. The Hengduan Mountains region has been recognized as being highly susceptible to landslides because of frequent earthquakes, extreme precipitation, and intensifying human activities [15,39,59,63].

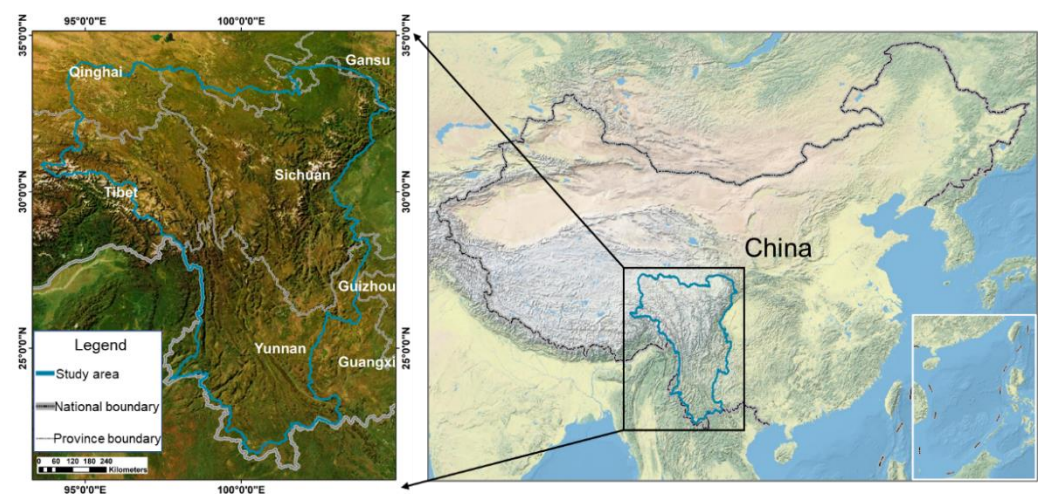


**Figure 1.** The study area is located in the SSW of China, with an area of more than 700,000 square kilometers.

## 3. Data and Methods

### 3.1. Data

#### 3.1.1. Landslide Inventories

A landslide inventory map contains valuable information about the spatial pattern of landslide events in any given region, enhancing the understanding of landslide behavior

and the LS evaluation. It is a critical step in LS studies to make a landslide inventory map [23]. Here, we obtained historical landslide data from Natural Resources Bureaus of eight administrative divisions, including Tibetan Qiang Autonomous Prefecture of Ngawa, Diqing Tibetan Autonomous Prefecture, Tibetan Autonomous Prefecture of Garzê, Nujiang of the Lisu Autonomous Prefecture, Liangshan Yi Autonomous Prefecture, Lijiang City, Nyingchi, and Ya'an, covering 74 districts and counties accounting for 48.59% of the Hengduan Mountains region area, with a total of 21,112 geological disaster points in three categories, i.e., landslide, rockfall, and debris flow. The period of landslides covers a period of 2000–2020. Here, we use the term “landslide” to describe rotational or translational mass movement slide type. However, a portion of the raw landslide data lacks geographic coordinates, time information of the landslides, and description information. Therefore, we exclude this part of landslide data with missing information, for reliability of the assessment results. After cleaning and eliminating data absent of attributes, a total of 7217 landslide locations (centroid) were obtained (Figure 2), and we named this landslide points dataset as Expedition Data. In addition, we collected landslide data from the Resource and Environmental Science and Data Center of the Chinese Academy of Sciences (<https://www.resdc.cn/> accessed on 10 July 2020), which covers the whole range of the study area and is mainly used for visual comparative verification of LS assessment results. We named this dataset as Investigation Data. The statistical time of expedition data and the investigation data were up to 2020. Due to different sources of landslide data, landslide surveys vary in detail and landslide inventories. Here, we use expedition data as training data for LS evaluation and investigation data as visual comparison data for evaluating performance.

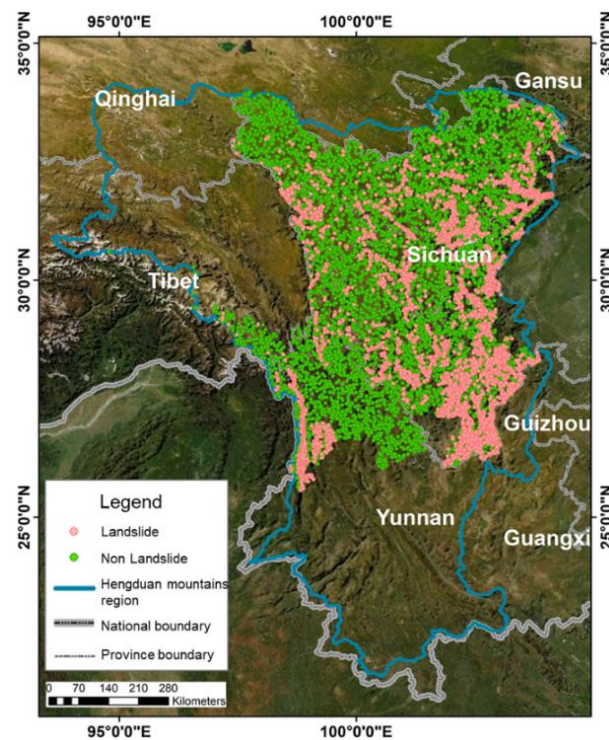


**Figure 2.** Landslide points obtained from Natural Resources Bureaus of eight administrative divisions after data cleaning. Non-landslide points used the Create Random Point module in ArcGIS.

### 3.1.2. Explanatory Variables

Selection of appropriate explanatory variables is a critical step in the LS assessment, but no commonly accepted selection criterion is available [40]. Based on landslide behavior across the Hengduan Mountains region [34,51,64,65], 50 explanatory variables were accepted as input variables for LS assessment. For the LS evaluation across the large-scale and

spatially heterogeneous region, we subdivided these explanatory variables into three categories, i.e., static, dynamic, and triggering factors [39,41,66]. The underlying surface-related explanatory variables that were related to sliding behaviors of landslides were taken as static factors [67,68]. Here, we defined dynamic factors as the explanatory variables derived from remote sensing images associated with dynamic changes in the underlying surface. Explanatory variables that trigger mass movements were called triggering factors [69], such as rainfall and earthquakes considered in this study. The explanatory variables are listed in Table A1.

Static factors involved 9 explanatory variables from DEM, road net, river net, and geology fault vector data. Elevation has been evidenced to be substantially viable in depicting spatial distribution of landslides [70]. Slope is an important factor for landslide processes, since it controls the shear forces acting on mountain hill slopes [19,71]. Aspect is associated with diurnal anisotropic heat, root development, weathering, and other geomorphological processes [72,73]. Curvature shows topographic relief that is considered to be a causative factor for landslide, which controls the convergence or divergence of landslide materials and water in the direction of landslide movement [23]. The terrain ruggedness index is an indicator of the variation of surface relief and the degree of erosion [25]. The topographic wetness index (TWI) reflects the effects of topography and soil characteristics on the spatial distribution of soil moisture [29]. The distance from fault indicates the likelihood of landslides induced by ruptures and fault surfaces easily become sliding surfaces because the stress on the rock surrounding a fault is unstable [74]. The distance from river and LS are in close interaction, and this distance indirectly describes the erosion power of streams, which plays an important role in landslides [24]. The distance from the road net is used as an indicator to measure landslides derived from or related to road construction [75].

Dynamic factors included 33 explanatory variables, which were obtained or calculated from Sentinel-1/Sentinel-2 and Landsat satellite data (Table A1). Satellite remote sensing data (SAR or optical data) have been widely used in landslide identification and spatiotemporal analysis of landslide activity [40,43,46,47,76]. In general, LS are identified by analyzing vegetation cover changes and relief-oriented parameters using different vegetation indices [77]. The texture of soil represents the relative proportion of sand, silt, and clay content, which is highly correlated with landslide susceptibility. In addition, landslide initiation shows close dependency to high soil moisture levels and low vegetation density [78–81]. Here, we use various vegetation indices to characterize the fingerprint characteristics of land cover changes and spectral-texture information relevant to landslides. The amplitude component of an SAR image is related to surface roughness, surface material, soil water, and radar polarization, which has a strong relation with landslide occurrence [76,82]. In order to better characterize the dynamic changes of surface material composition and soil water content, we used the amplitude data of SAR with different polarization methods and calculated the spatial correlation of information after data smoothing [83,84]. In this study, we integrated optical and SAR satellite data incorporated with extracted index information and Geary's C spatial analysis information to delineate the dynamic change process of the underlying surface (Table A1). Considering the diversity of dynamic factors and remarkable value ranges of the dynamic factors, we normalized the dynamic factors before further analysis.

Triggering factors are mainly rainfall and earthquakes in this study area, according to the hazard property information of landslide inventories. Quantile level analysis of precipitation data can reflect the precipitation characteristics of the study area [85]. Here, we used the distance from the epicenter and precipitation percentiles to determine the spatial clustering of landslides [8,86].

### 3.2. LS Assessment Framework

The LS assessment framework proposed in this study is based on binary classification over the study area through pixel-by-pixel calculation, which was separated into four phases: (a) preparation of training and validation sample data, (b) construction of data

features, (c) comparison of the selected three LS assessment models, and (d) mapping of the LS across the study region (Figure 3).

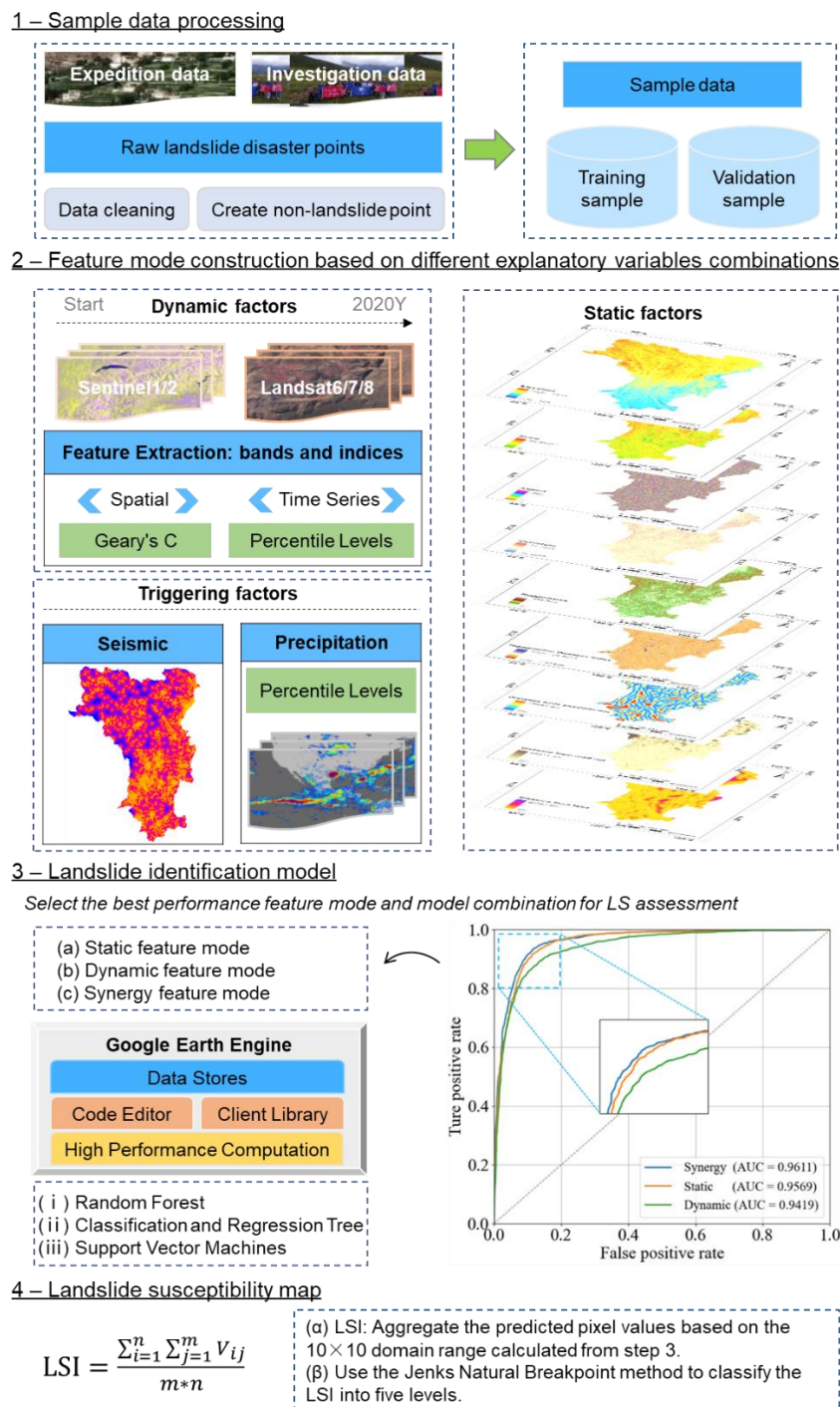


**Figure 3.** Schematic overview of LS evaluation framework. Specific processing steps for each part (1–4) are listed in a dashed box. All explanatory factors are listed in Table A1.

### 3.2.1. Sample Data

The LS assessment model requires both landslides, denoted as 1, and non-landslides, denoted as 0 [87]. The expedition landslide inventory data of 7217 landslide sites were taken as positive samples. Here, we used the Create Random Point module in ArcGIS to generate non-landslide samples for further modeling [16]. Two strategies were adopted to avoid a blind selection of data points introducing uncertainty into the model training procedure

which may produce an unreliable LS assessment. At first, the spatial range of generated random points should be in consistency with these eight municipalities where expedition data were collected. Second, random points within a 1 km buffer zone from landslide positive samples were screened out. At last, 7218 non-landslide points were generated as negative samples. The ratio of landslide and non-landslide samples is determined as 1:1 [19]. Thus, a total of 14,435 samples were produced for LS assessment. Sample data were randomly split into dataset for model training (70% of the total dataset) and model verification (30% of the total dataset) [88].

### 3.2.2. Development of Feature Modes

We grouped explanatory variables into three feature modes for LS assessment, i.e., static mode, dynamic mode, and synergy mode. Static factors and triggering factors were combined to form the static mode; combination of dynamic factors and triggering factors formed the dynamic mode; and the integration of static factors, dynamic factors and triggering factors formed the synergy mode. Triggering factors are those factors that cause mass movements, so we added triggering factors for different data modes. A set of performance metrics for different feature mode testing was recorded during mode validation using the RF method. Then, the feature mode with the highest modeling performance was used to map LS. The preparation of the feature modes includes the calculation of static factors and dynamic factors. The static factors were calculated through ArcGIS and SAGA GIS software and then uploaded to GEE LEGACY ASSETS. The calculation of dynamic factors is implemented in GEE by coding and then stored in GEE LEGACY ASSETS.

### 3.2.3. LS Assessment Model

Three classifiers were chosen for LS assessment, i.e., Random Forest (RF), Classification and Regression Tree (CART), and Support Vector Machines (SVM). Our analysis based on these three classifiers was done via GEE, allowing large-scale predictions at the pixel scale [57].

RF classifier is an efficient and optimal in computation performance in dealing with high dimensionality of data [89], which has been widely used in satellite-based applications [28].

CART is a rule-based algorithm that splits the dataset subsets using all predictor variables to create two child nodes repeatedly, and the predicted value of a “terminal” node is the average of the response values in that node [90]. Predictor variables can be of any type (numeric, binary, categorical, etc.), and model outputs cannot be influenced by monotone transformations and different scales of measurement among predictors [91–93].

SVM, a kernel-based algorithm for classification and regression issues, has been widely used in LS mapping [19,94]. For nonlinear feature datasets, as in LS modeling, SVM is used to project features into high dimensional space with kernel functions, allowing classification within a plane [95].

We verified these three classifiers using the same feature mode. A set of performance metrics for testing were recorded for comparison of these classifiers. Then, a model selected with the highest modeling performance and the well-chosen feature mode were used to map the LS over the Hengduan Mountains region.

### 3.2.4. LS Mapping

The landslide identification model developed here was used to analyze the spatial pattern of landslides at the pixel scale with a spatial resolution of 30 m. LS is strictly a classification problem, with the binary outcome of presence or absence of a landslide [96]. The predicted value of 1 means that landslides will occur within the pixel range, and the predicted value of 0 means no landslides within the pixel range. The high spatial resolution of 30 m of the predicted result allows us to better identify the fingerprint of landslides [13]. Besides, whether or not landslide occurs at a given location is closely related to the triggering factors within and in the proximity of the regions with the occurrence

of landslides. To construct the landslide susceptibility map, two main steps should be followed: first generate the landslide susceptibility indexes (LSIs), and then reclassify the LSIs. Here, we aggregated the predicted landslides and summed the pixel values of landslides based on the  $10 \times 10$  domain range. So, we obtained a 300 m resolution spatially aggregated raster image, at which the size of the image element values indicates the occurrence possibility of landslides within a  $300 \text{ m} \times 300 \text{ m}$  range (Equation (1)). The abovementioned processing procedure can well avoid the subjective judgment error of the model-based assessment results and can better reflect the trend of landslide occurrences through statistical characteristics of landslides within a specific region. Finally, we used the Jenks Natural Breakpoint method to classify the LS into five levels, seeking to minimize the differences within levels and maximize the differences between levels [11,29]. Here, we classified the LSI into very low LS, low LS, medium LS, high LS, and very high LS:

$$\text{LSI} = \frac{\sum_{i=1}^n \sum_{j=1}^m V_{ij}}{m \times n} \quad (1)$$

where  $m$  and  $n$  are the row and column number of LS assessment unit, respectively, with spatially aggregated  $10 \times 10$  domain range.  $V_{ij}$  is the predicted pixel value corresponding to row  $i$  and column  $j$ .

### 3.3. Validation of LS Assessment Framework

The expedition landslide data collected through field survey and the investigation landslide data mapped by Chinese Academy of Science (CAS) were used to validate the LS assessment framework proposed in this study. Expedition landslide data was divided into training data and validation data. The training data were used for the development of the model and the validation data were used for the selection of the model. Here, we used the receiver operating characteristic curve (ROC) and area under curve (AUC) to evaluate and compare the effects of different feature modes on the LS map [97,98]. The algorithm used in this study included binary classification, confusion matrix, and statistical indicators (i.e., precision, accuracy), which were adopted to quantitatively compare the accuracy of LS assessment models [99]. In binary classification, the accuracy is the proportion of correct predictions (both true positives and true negatives) among the total number of cases, while precision is the ratio of true positives to the total of the true positives and false positives. The formula is:

$$\text{Accuracy} = (\text{TP} + \text{TN}) / (\text{TP} + \text{TN} + \text{FP} + \text{FN}) \quad (2)$$

$$\text{Precision} = \text{TP} / (\text{TP} + \text{FP}) \quad (3)$$

where TP = true positive; FP = false positive; TN = true negative; and FN = false negative.

Investigation landslide data mapped by CAS delivers valuable information on the spatial pattern of landslides in the landslide susceptible zone. Then, we used the investigation landslide data to compare the modeling results from a macro perspective and to qualitatively measure the spatial consistency of the LS maps.

## 4. Result

### 4.1. Development Environment of Landslides

The spatial pattern of triggering factors behind landslides can decide the spatial patterns of landslides. Therefore, we depicted the spatial pattern of triggering factors behind landslides. Static factors included nine explanatory variables (Figure 4). The topography of the Hengduan Mountains region is generally high in the north and low in the south, with remarkable differences in terrain, which cause unstable mountain slopes. The mountains run generally in a north–south direction between  $25^\circ$  and  $30^\circ\text{N}$ , with a slight tilt toward the west at their northern end and a tilt toward the southeast at their southern end (Figure 4a). The slope, curvature, and roughness delineate the topographical changes, which are consistent with the undulations of the mountains (Figure 4b–d). The aspect has no distinctive spatial characteristics (Figure 4e). TWI is higher at the relatively

low-lying terrain (Figure 4f). The distance from the road net indicates a higher density of road networks in the southern parts of the study region and, hence, a higher intensity of human activities (Figure 4h). Large rivers are all developed parallel to the faults and deep major fractures and are densely distributed throughout the study area (Figure 4g,i).

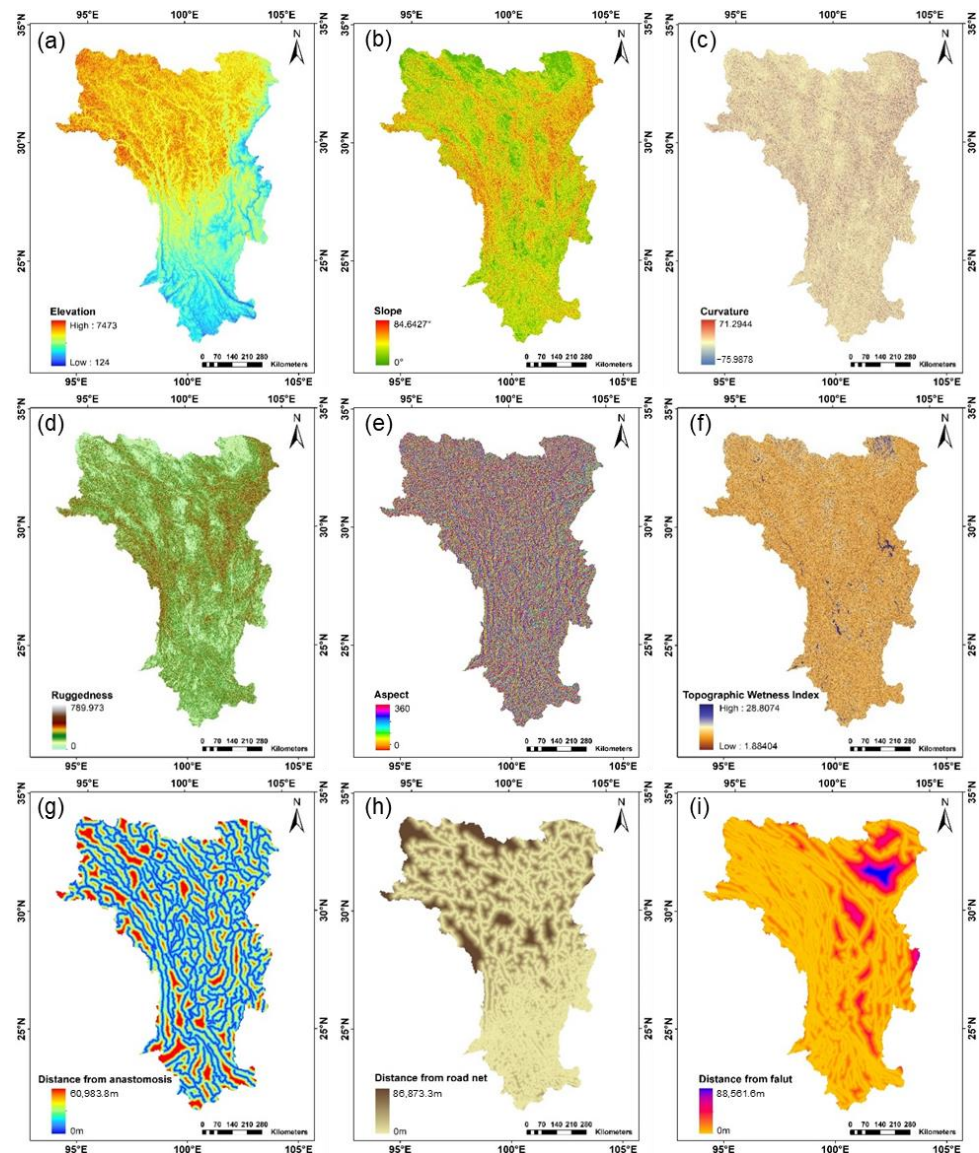


**Figure 4.** Static factors preselected: (a) elevation; (b) slope; (c) curvature; (d) terrain ruggedness index; (e) aspect; (f) topographic wetness index; (g) distance from anastomosis; (h) distance from road net; (i) distance from fault.

Dynamic factors included 33 explanatory variables (Table A1), and we analyzed the dynamic factors of the landslide and non-landslide sample points (Figure 5). Before further analysis, we normalized the dynamic factors considering the diversity of dynamic factors and remarkable value ranges of the dynamic factors. The quartiles of dynamic factors of the landslides are larger than those of the non-landslides, implying large differences in the eigenvalues of the samples throughout the study region. For Geary's *C* spatial analysis, the values of both landslide and non-landslide factors mostly ranged from 0 to 0.1, which are much smaller than 0.5, indicating a strong spatial correlation of landslides and homogeneous features within the domain of landslides. Therefore, it is an ideal protocol for remote-sensing-based identification of landslide hazards in the Hengduan Mountains region.

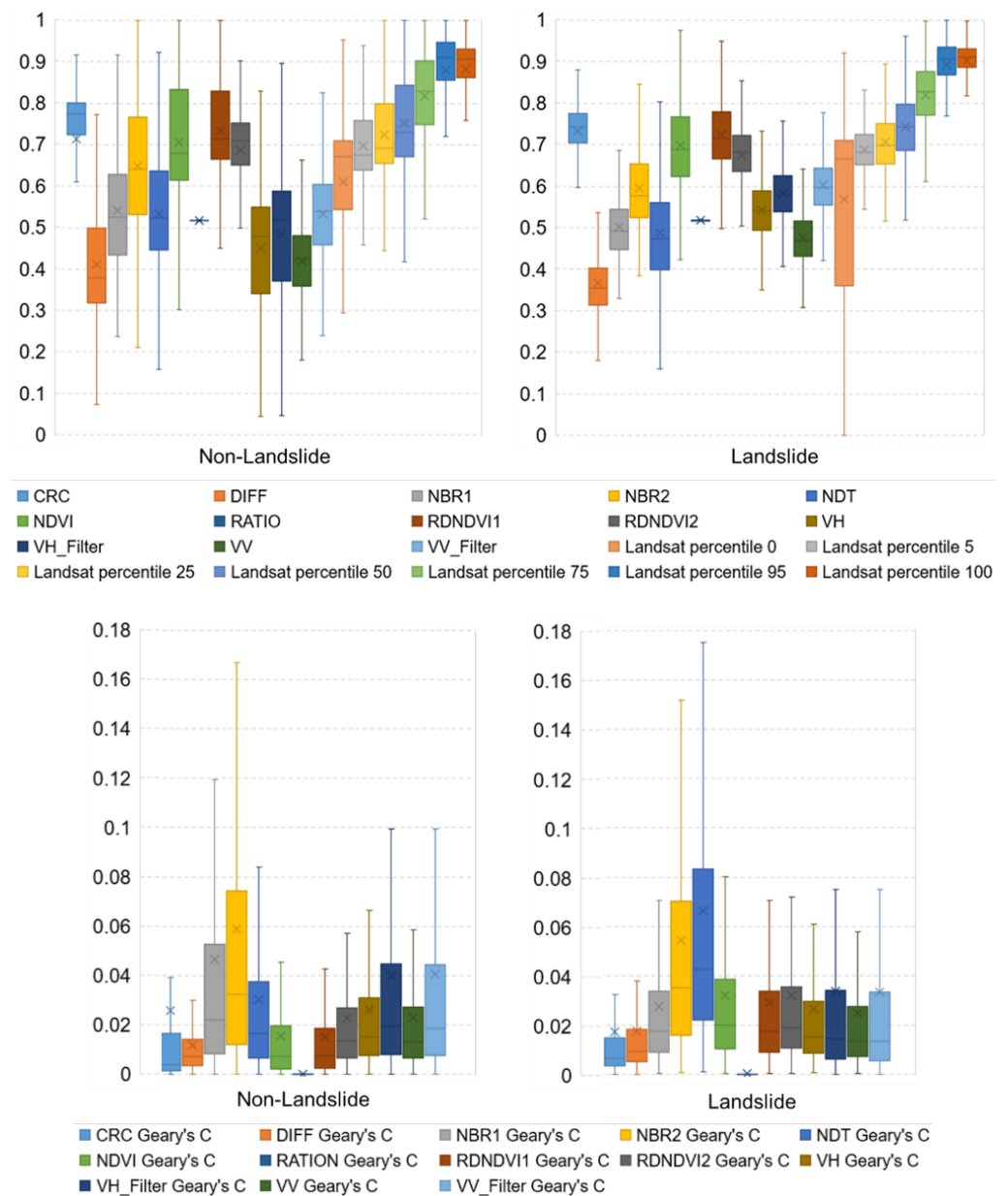


**Figure 5.** Statistical box plots of dynamic factors.

#### 4.2. Performance Evaluation of LS Assessment Models

Results of the machine learning method are heavily reliant on the quality of the selected feature data and the merits of the algorithms. The evaluation of LS assessment models included two steps, i.e., comparison of various feature modes and comparison of different algorithm performances.

##### 4.2.1. Feature Modes Comparison

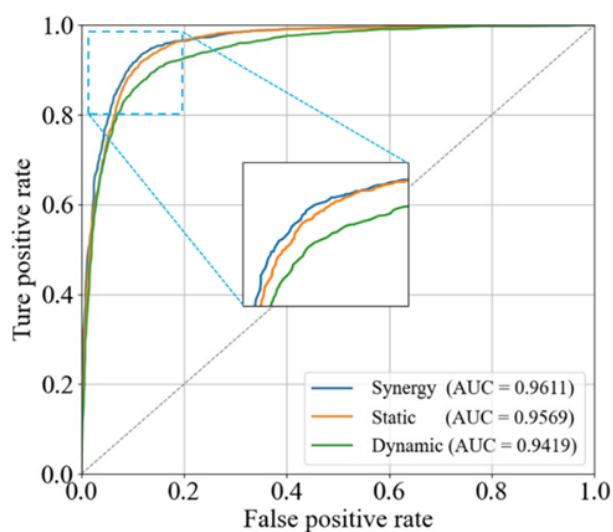
The RF model was chosen to compare and analyze the landslide assessment results by different feature modes. To assess the importance of each feature mode, given a pre-scribed set of hyperparameters, three feature modes were used separately with the RF model to identify the landslides: (1) static mode, (2) dynamic mode, and (3) synergy mode. We used the hyperparameters numOfTrees = 200, variablesPerSplit = 'sqrt', and min\_samples\_leaf = 1 when implementing the model in GEE [100].

Figure 6 shows the accuracy and performance metrics of the LS assessment obtained with three different feature modes, i.e., static mode, dynamic mode, and synergy mode.

The validation results showed 0.9611 for the synergy model AUC, 0.9569 for the static model AUC, and 0.9419 for the dynamic model AUC. In addition, the accuracy indices calculated by the confusion matrix showed 90.48% in accuracy and 89.24% in precision for the synergy model, 89.74% in accuracy and 87.30% in precision for the static model, and 87.39% in accuracy and 83.80% in precision for the dynamic model. All these statistical metrics showed that the assessment model using synergy mode had higher evaluation accuracy and better performance. The results indicated that the paradigm of the leverage synergy mode combined with the machine learning algorithm based on the GEE platform for large-scale LS assessment was viable and feasible and had a satisfactory assessment performance.

Static Confusion Matrix		Predicted Label		Dynamic Confusion Matrix		Predicted Label	
		P	N			P	N
True Label	P	1926	159	True Label	P	1827	258
	N	280	1915		N	281	1911
Synergy Confusion Matrix		Predicted Label		Mode	Acc	Pre	
		P	N	Static	89.74%	87.30%	
True Label	P	1908	177	Dynamic	87.39%	83.80%	
	N	230	1962	Synergy	90.48%	89.24%	

(a)



(b)

**Figure 6.** Assessment accuracy comparison and performance analysis of different feature modes: (a) evaluation metrics, top-left: static model confusion matrix, top-right: dynamic model confusion matrix, bottom-left: synergy model confusion matrix, bottom-right: accuracy indices; (b) ROC curve of synergy, static, and dynamic feature modes.

#### 4.2.2. Comparison of Landslide Identification Performances of Models

We determined that synergy mode with the machine learning algorithm was the right choice for further LS assessment practice. To do LS assessment with higher accuracy, we compared three types of classifiers for modeling performance, and the classifier with the highest modeling performance would be adopted for LS mapping over the study region.

Figure 7 showed the accuracy and performance metrics of the LS assessment using three different classifiers, i.e., RF, CART, and SVM. The accuracy indices calculated by the confusion matrix showed 90.48% in accuracy and 89.24% in precision for the RF classifier, 84.80% in accuracy and 84.75% in precision for the CART classifier, and 72.20% in accuracy and 66.83% in precision for the SVM classifier. Evaluation metrics showed that the RF classifier had the best performance and highest accuracy when compared to CART and SVM. In addition, we perform LS mapping using CART and SVM classifiers to get the spatial performance. Through visual interpretation, it can be seen from LSM that there is a common overfitting phenomenon in CART and SVM (Figure A1). In this case, we developed a LS assessment paradigm at the regional scale, i.e., the RF classifier coupled with synergy feature mode using the GEE platform for LS assessment.

RF Confusion Matrix		Predicted Label	
		P	N
True Label	P	1908	177
	N	230	1962

(a)

CART Confusion Matrix		Predicted Label	
		P	N
True Label	P	1750	335
	N	315	1877

(b)

SVM Confusion Matrix		Predicted Label	
		P	N
True Label	P	1779	306
	N	883	1309

(c)

Mode	Acc	Pre
RF	90.48%	89.24%
CART	84.80%	84.75%
SVM	72.20%	66.83%

(d)

**Figure 7.** Assessment accuracy comparison and performance analysis of different models. (a) RF model; (b) CART model; (c) SVM model; (d) accuracy indices.

### 4.3. Spatial Pattern of LS

The LS map obtained by the assessment methodology (Figure 8a) indicated free LS in the northern part of the Hengduan Mountains region. The areas without LS colors mean the aggregation result value is zero. In addition, we take a zero LS value as the background, which indicates that landslides in these areas are unlikely to occur. These areas include, but are not limited to, flat land and bodies of water such as lakes (Figure A3). Most high or very high LS levels can be attributed to unstable slope bodies due to weathering and/downcutting of the river channel, while downcutting processes can also be motivated by road construction. Besides, intensifying human activities also intensify the weathering processes of rocks and soils. The LS level is usually higher along the road than the surrounding areas, and potential human activities, mainly the construction of roads, have modified the stability of slope and induced landslides (Figures 9–14). We found higher LS in the southern parts of the study region when compared to that in the northwestern region, while population density and economic activities in the southern region had the dominant contribution to higher LS. The density of road network (Figure 4) also showed that the roads in the southern part of the study area were subject to higher density, and these regions matched well the regions with high LS, implying a considerable fractional contribution by human activities to LS in the study region.

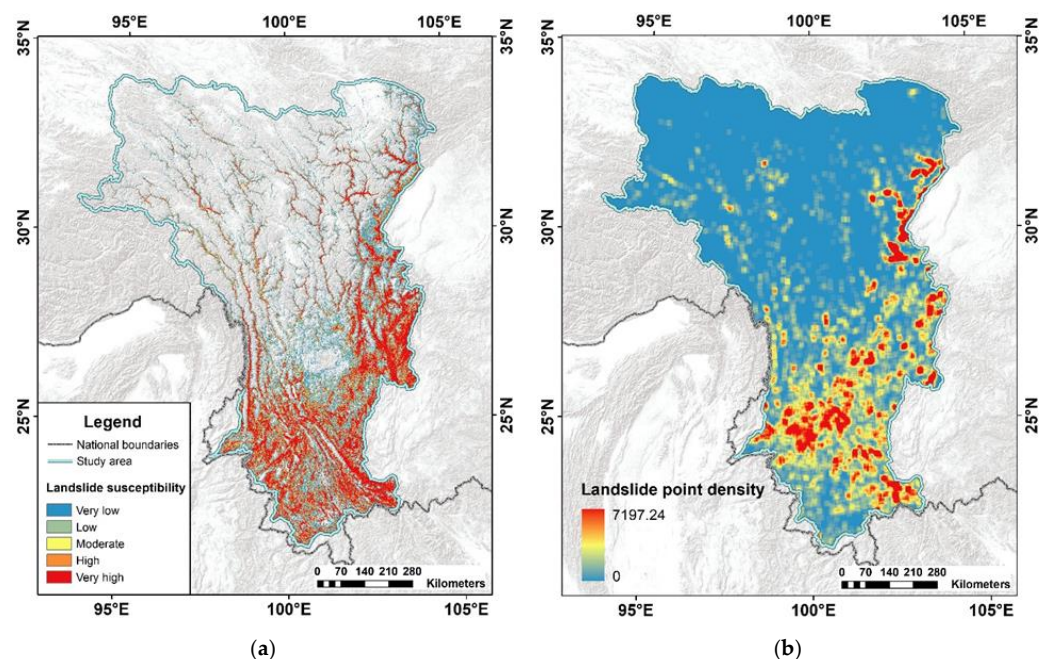


**Figure 8.** Landslide susceptibility assessment results and comparison with investigation landslide data. (a) Landslide susceptibility map; (b) landslide point density map based on the data of Resource and Environment Science and Data Center of the CAS.

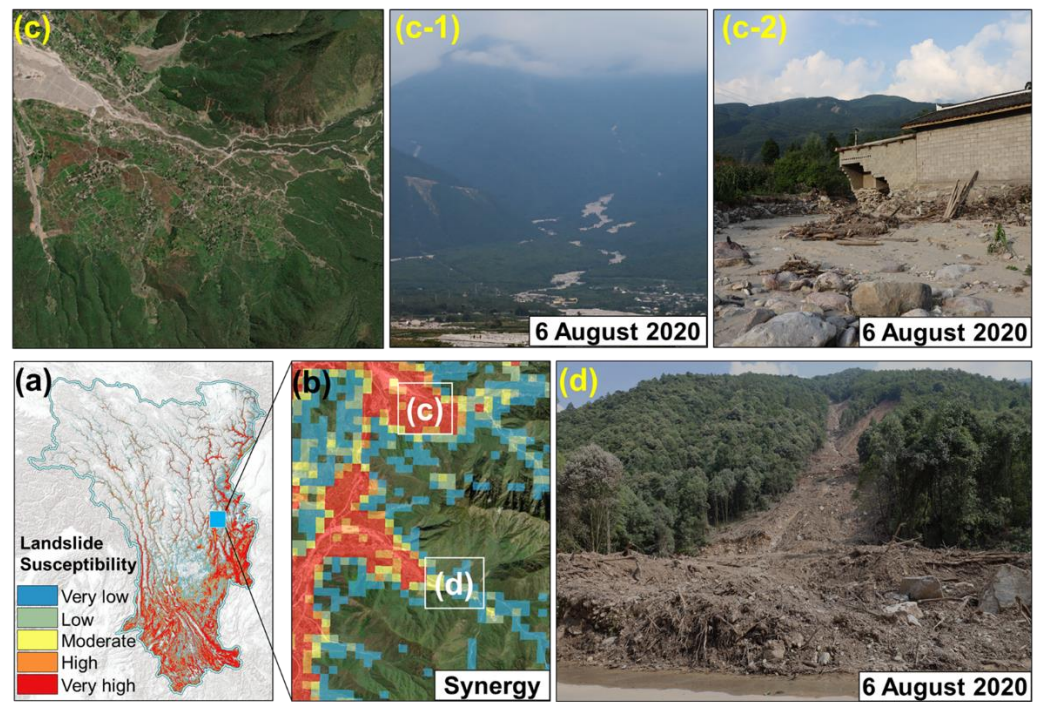


**Figure 9.** The landslide susceptibility of the central Hengduan Mountains. (a) is the LS map of the Hengduan Mountains region; (b) shows the landslide assessment result of this area; (c,d) are field photos showing the geological disasters that happened at different sites; (c-1) is a close-up view of c, and (c-2) is a detailed picture of the landslide disaster.

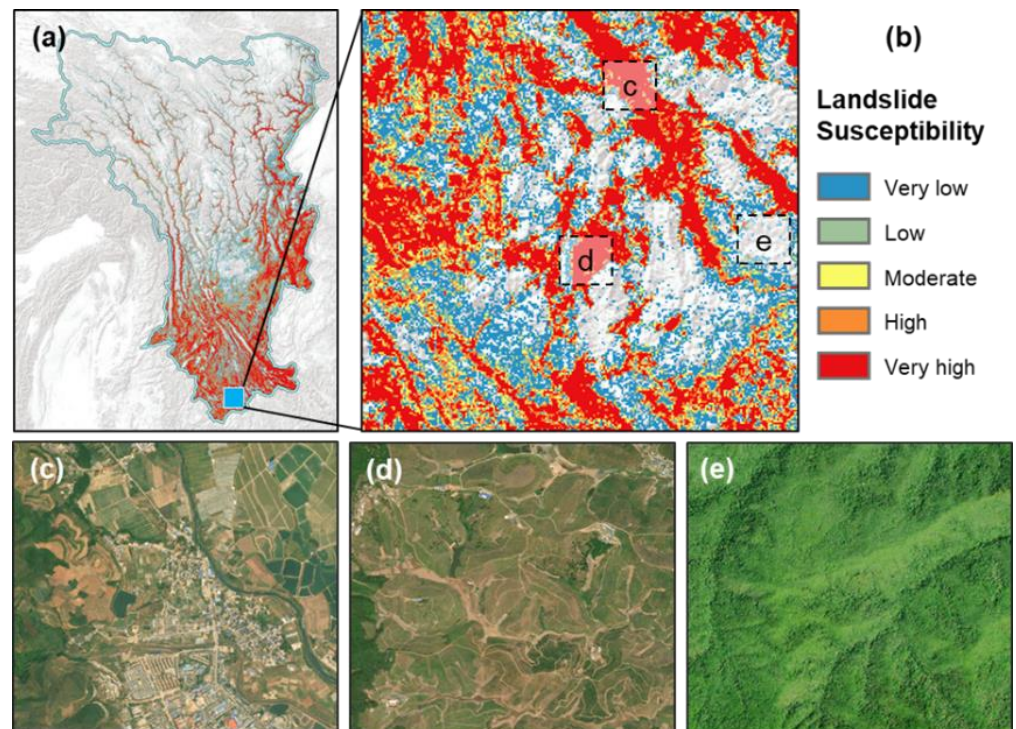


**Figure 10.** Verification and evidence for LS map over the Hengduan Mountains region. (a) The landslide susceptibility classification; (b) landslide susceptibility in the southern part of the area. Panels of (c–e) show Esri satellite imagery with different land covers: (c) human settlements, (d) terrace, and (e) forest area.

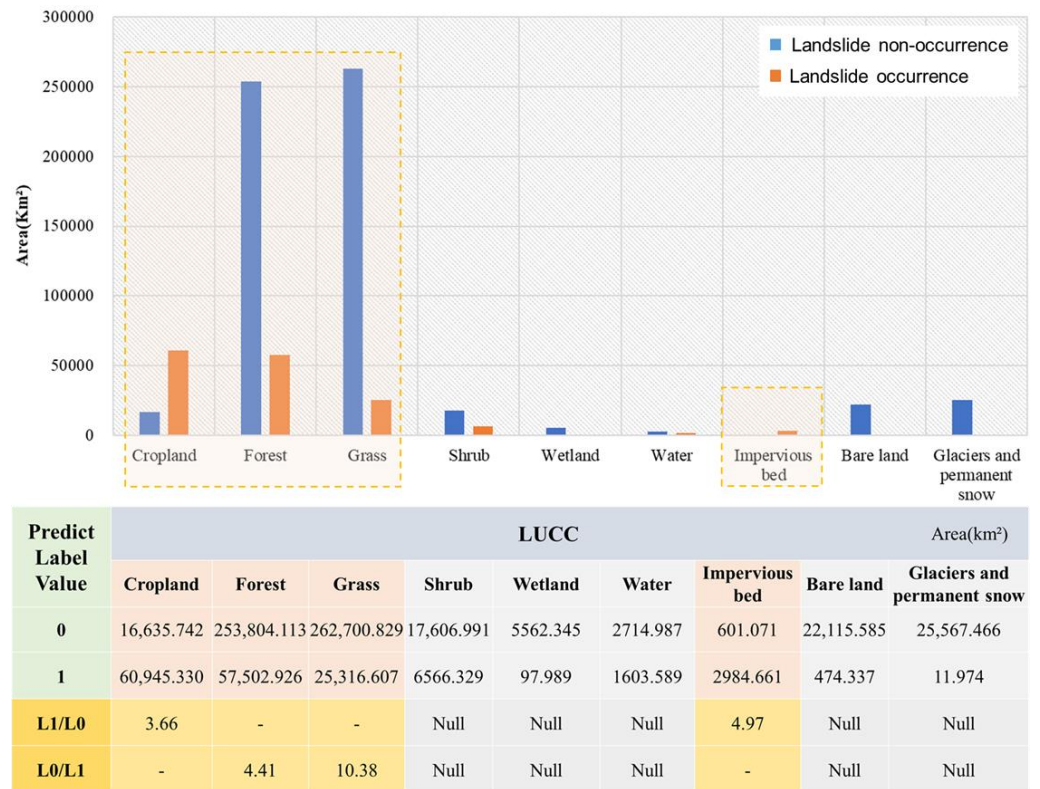


Figure 11. Landslide susceptibility assessment results and comparison with investigation landslide data. Predict label values 0 and 1 represent landslide non-occurrence and landslide occurrence respectively.

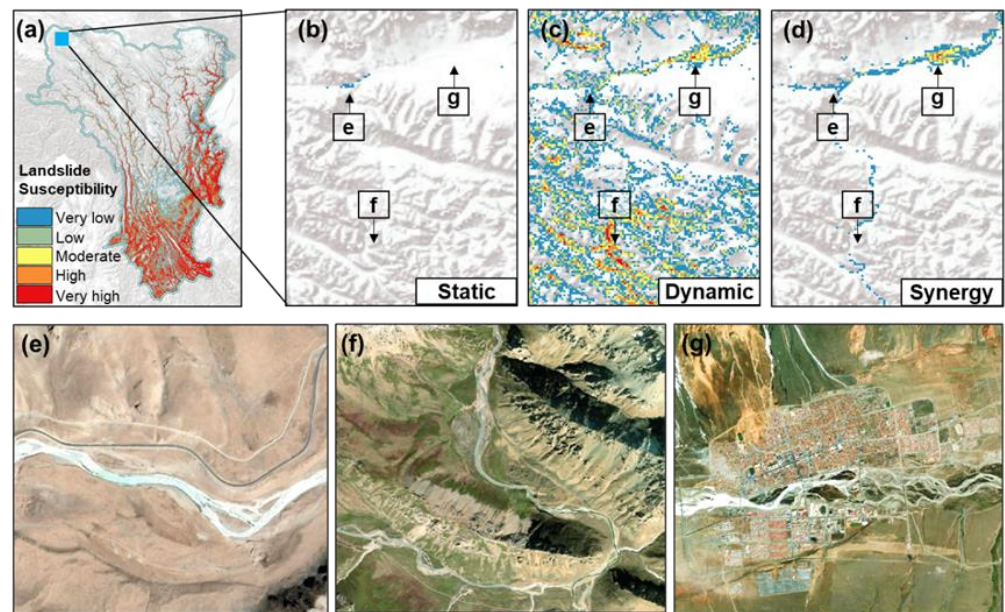
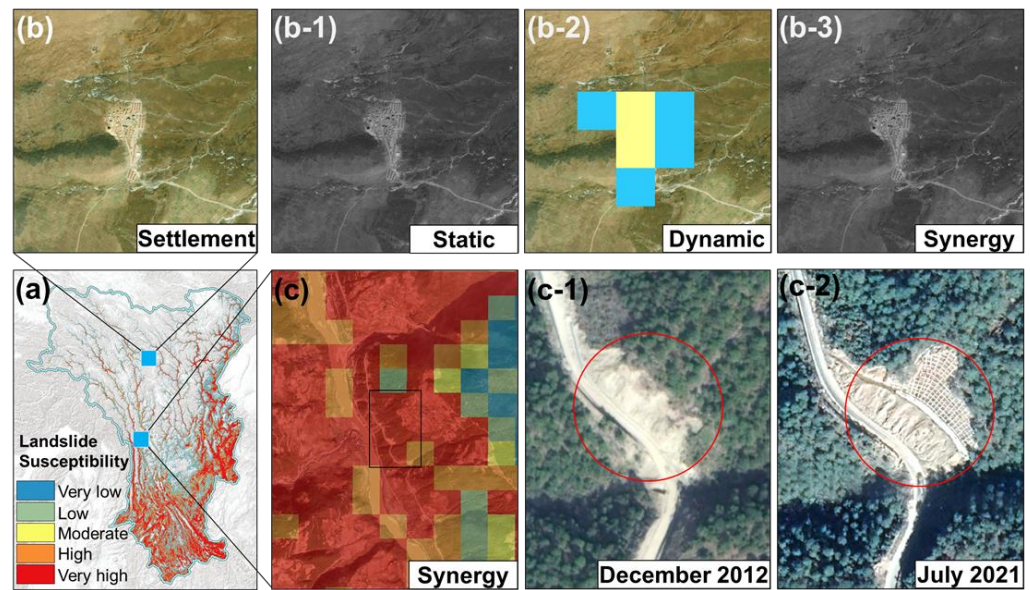
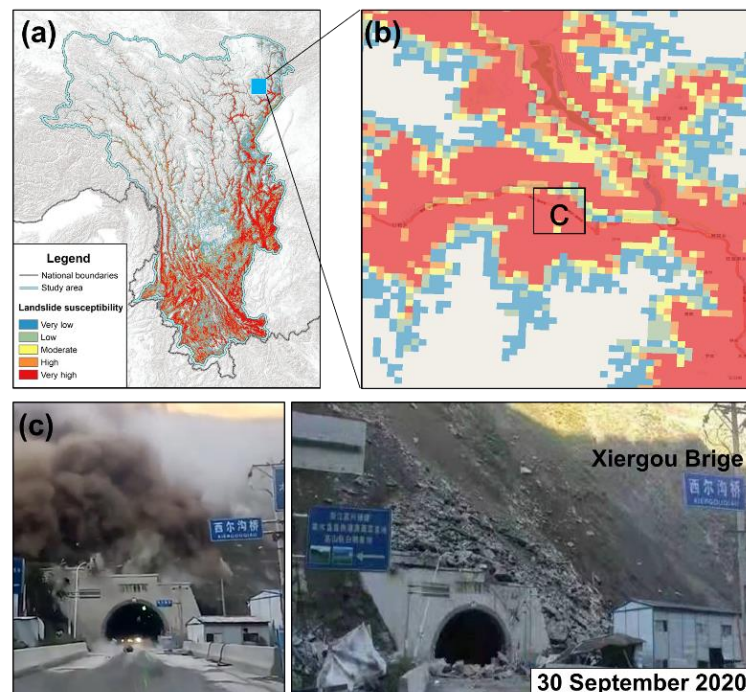


Figure 12. The LS of the northern transverse mountain area. (a) is the landslide susceptibility map of the Hengduan Mountains region. (b–d) show the similarities and differences of LS assessment results in static feature mode, dynamic feature mode, and synergy feature mode. (e–g) display details using Ersi and Google satellite image. Dynamic feature mode can sense detailed information of the pregnant environment, but the identification of floodplain fans and moraine landscapes can be easily confused. However, the synergy feature mode is beneficial to improve recognition accuracy.



**Figure 13.** The LS of the central transverse mountain area. (a) is the LS map of the Hengduan Mountains region. (b) shows different LS assessment results in static feature mode (b-1), dynamic feature mode (b-2), and synergy feature mode (b-3). (c) displays details of a site prone to landslide using Ersi and Google satellite image; (c-1) shows early sign of landslide and (c-2) shows an recently constructed artificial slope protection building. Results show that using the dynamic feature mode can identify spatial texture structure information, and, when combined with static feature mode, it can reduce the false alarm rate and ensure the reliability of results.



**Figure 14.** LS assessment results and comparison with landslide disaster information obtained from the Internet media. (a) is the LS map of the Hengduan Mountains region. (b) is the zoom-in view of LS map. (c) shows the scene when the landslide occurred.

From the results of LS assessment in the study area, regions with high LS were in agreement with the spatial pattern of the landslide hazard density map produced from the investigation dataset by the Resource and Environment Science and Data Center of

the Chinese Academy of Sciences (Figure 8b). It should be noted that the landslide point density map could not locate every landslide hazard point. Here, we show a couple of possibilities. (1) The landslide hazard occurred a long time ago, and now we cannot identify it due because the traces of landslides disappeared due to long-term weathering and vegetation coverage changes. In this case, the landslide point density map might omit these obliterated landslide disaster relics. (2) The landslide/landslides occurred but this/these landslide event/event(s) were not recorded. It could be because these landslide locations were inaccessible. Thus, the landslide locations recorded by the landslide point density map can be modeled by the LS assessment framework proposed in this study, implying that the modeling performance of the framework is acceptable. The proposed framework can locate other landslide locations that were not recorded in the landslide point density map. The density map of the training data used in the proposed framework is shown in Appendix B Figure A2. Hence, the modeling results can provide unique and irreplaceable information for enhancing mitigation of landslide disasters over the study region and can provide the reference information for the evaluation of landslide susceptibility in other regions of the globe.

## 5. Discussion

In this study, we developed a framework for assessing LS at the regional scale, allowing the efficient assessment of spatiotemporal variations in LS at a finer spatial resolution with the timely update of data, which is a kind of breakthrough into timely and systematic landslide susceptibility evaluation in regions with enormous difference in terrains. Based on the GEE platform and a synergy feature mode for comprehensively utilizing static and dynamic explanatory variables, our approach provides discernment of potential landslide locations, where landslides are subject to higher occurrence probability in a timely way. In this sense, the LS assessment framework can provide a viable technique for mitigation of landslide risk.

For machine learning methods for assessments of landslide susceptibility, the reliability of the model is closely related to the training sample, that is, the landslide inventory [14]. However, a landslide inventory cannot include all landslides occurred over a given region. Here, we used two inventories of landslide from different agencies to ensure acceptable representation of spatiotemporal pattern of landslides over the study region, i.e., expedition data were used for training samples and investigation data were used for comparison of the LS assessment map.

Availability of high-quality multisource and extensive data is a must to achieve an acceptable spatial assessment of LS [101]. Therefore, a synergy of static factors representing topography proxies and dynamic factors related to Earth surface properties and dynamic changes was used to identify landslide prone area over large-scale regions dominated by spatially heterogeneous geographical and geological features. Besides basic topographical and hydrometeorological features (Table A1), we further integrated various vegetation indices (i.e., NDVI, CRC, etc.) and spatial structure elements (Geary's C test) to derive landslide-related vegetation changes and diagnostic features [43,58]. Synergy feature mode combines the advantages of both types of data features, which reduces the noise error introduced by static feature mode or dynamic feature mode and can better represent the hazard-pregnant environment. Moreover, application of the proposed feature mode revealed that the LS assessment model using synergy mode achieved the highest modeling accuracies, when compared with the LS assessment model with static or dynamic feature mode only (Figure 6). Then, we compared machine learning algorithms based on the synergy feature mode and found that the RF algorithm had a better performance and generalization ability and the modeling accuracy reached 90.48% and precision reached 89.24% (Figure 7). An improved framework integrating multiple explanatory variables with the fine spatial resolution ensured a reliable LS assessment with respect to the occurrence of landslide (Figure 9). Aforementioned procedures can help to produce a LS map using synergy feature mode, which can be put into practice (Figure 9a).

The LS assessment paradigm was designed to facilitate landslide research with a finer spatial resolution at the regional scale. We found that our modeling results were in agreement with the existing findings [7,15,59]. However, we can better identify the subtle spatial differences of the LS within the study area in a near-real-time way based on the GEE platform. Due to a large spatial range of the study region, the study region is dominated by discernible spatial heterogeneity in geomorphology, hydrometeorology, and triggering factors and the resulting distinctly variable LS in both space and time. Regions with a higher LS across the northern parts of the study region are spread along rivers, roads, and large fractures (Figure 8a), while a relatively high LS can be found over the southern part of the study area, which is attributed mainly to unstable slopes due to interferences of human activities such as an interwoven road network, a widespread residential area, and croplands (Figure 10).

In high-latitude mountains, the stability of colluvial slope bodies is highly sensitive to external interferences or external forces, such as road construction, land reclamation, rainstorms, and so on. Different external forces may cause different degrees of instability of the colluvial slope bodies. In this case, we quantified percentages of landslide and non-landslide areas over regions with different land-use types. We found that non-landslide areas were 4.41 times and 10.38 times more than the landslide areas in the forest and grassland land types, respectively, while the landslide areas were 3.66 times and 4.97 times higher than the non-landslide areas in the cropland and impervious surface land types, respectively (Figure 11). These findings evidenced close relations between land use changes and LS in both space and time, illustrating a large spatial heterogeneity in LS variations that is highly influenced by forest cover types, cropland shifts, and settlement patterns [102–104].

Aiming to further verify and evidence LS assessment results, we did field surveys across the Hengduan Mountains region with a focus on typical landslides. Besides, we also attempted to obtain evidence from remote sensing images for additional evidence (Figures 9 and 11–14). Specifically, Figures 9, 12 and 13 describe the impact of use different feature mode on the LS results. Dynamic feature mode can sense detailed information of the pregnant environment and identify spatial texture structure information, but the identification of floodplain fans and moraine landscapes can be easily confused. However, the synergy feature mode is beneficial to improve recognition accuracy, reduce the false alarm rate, and ensure the reliability of results (Figures 12 and 13). Furthermore, we compare LS assessment results with landslide disaster information obtained from the internet media. The LS level of the area where the landslide occurred had high susceptibility, indicating that the quality of the LS assessment result is reliable (Figure 14). We carefully compared evidence from field surveys and remote sensing images and found that the LS assessment results of the proposed LS evaluation framework predicted and/or simulated the landslide locations with satisfactory accuracy and high reliability. We also compared the LS map with the landslide inventory data density map (Figure 8a). Since the landslide inventory data were collected from different sources, they provided a great opportunity for cross validation. It was interesting to find that the LS was well consistent with the density map of landslide point in the spatial pattern. Ongoing LS studies at the regional scale will benefit from improved confidence in the LS assessment framework.

## 6. Conclusions

With the consideration of complicated driving factors behind landslide disasters and particularly the damaging impacts of landslides on the infrastructure, human settlements, and socioeconomy in the mountainous regions, we proposed a novel holistic landslide susceptibility evaluation framework to map the LS by a synergy of static, dynamic, and triggering factors using the GEE platform and RF model. Here, we considered the Hengduan Mountains region as a case study region, since it is dominated by remarkable differences in terrain (>7000 m in difference of terrain), different land-use patterns, and high sensitivity to weather extremes. Frequent landslide disasters and relevant disastrous consequences, par-

ticularly, call for mitigation of landslide disasters in mountainous regions in the backdrop of warming climate. The proposed LS assessment framework involving landslide-related external and internal factors has been shown to be an effective technique for LS mapping in a near-real-time way, by routinely updating satellite data based on GEE's high-performance computing and abundant satellite data resources.

We mapped the LS over the landslide-prone Hengduan Mountains region with an area of ~700,000 km<sup>2</sup> in Southwest China and found that this LS assessment framework worked well in mapping LS at a finer spatial scale and hourly time scale. We also showed reliability and accuracy of the LS map over the Hengduan Mountains region via comparison between multisource landslides inventory data, remote sensing images, and the LS map by the proposed framework, which showed a match with these data. Besides, landslides by field surveys also corroborated the modeling results. The results indicated that the spatial patterns of forests and grasslands had a significant controlling effect on the spatial patterns of the occurrence of landslides, while human interferences due to road construction, land reclamation, and pasturing further triggered instability of the colluvial slope bodies, which could easily trigger the occurrence of landslides within the Hengduan Mountains region. The LS map showed a complete picture of the susceptibility of landslide disasters, providing valuable information of the location of the landslide-prone regions, and is, therefore, beneficial for preparedness for and mitigation of landslide risk.

The LS assessment framework is transferrable and can be used in other landslide-prone regions in the globe. Landslide hazards in mountainous regions can be expected to occur with higher frequency due to intensifying weather processes, intensifying human interferences, and accelerating melting processes of the permafrost layers in high-altitude regions, such as the Hengduan Mountains region. Reliable and timely LS mapping is necessary for the preparedness for and mitigation of landslide disasters in a warming climate.

**Author Contributions:** Conceptualization, W.W. and Q.Z.; methodology, W.W.; software, W.W.; validation, W.W. and Q.Z.; formal analysis, W.W.; investigation, W.W. and J.Z.; data curation, W.W.; writing—original draft preparation, W.W. and Q.Z.; writing—review and editing, W.W., Q.Z., V.P.S., G.W., J.Z., Z.S. and S.S.; visualization, W.W.; funding acquisition, Q.Z. All authors have read and agreed to the published version of the manuscript.

**Funding:** This research was funded by the China National Key R&D Program, grant number 2019YFA0606900.

**Data Availability Statement:** Not applicable.

**Acknowledgments:** We are thankful to the Bureau of Natural Resources in Yunnan, Sichuan, Qinghai, and Tibet for their assistance in the collection of the data analyzed in this study.

**Conflicts of Interest:** The authors declare no conflict of interest.

## Appendix A

**Table A1.** Landslide explanatory variables.

Categories	Explanatory Variables	Description and Processing of Data	Data Sources/Data Period
Static Factors	Elevation	DEM, Spatial resolution 30 m	NASA STRM V3
	Slope	Calculated by DEM	NASA STRM V3
	Aspect	Calculated by DEM	NASA STRM V3
	Curvature	Calculated by DEM	NASA STRM V3
	Terrain ruggedness index	Calculated by DEM	NASA STRM V3
	Topographic wetness index	Calculated by DEM	NASA STRM V3
	Distance from fault	Euclidean distance	China Geological Survey
Distance from anastomosis	Euclidean distance	Open Street Map	
Distance from road net	Euclidean distance	Open Street Map	

Table A1. Cont.

Categories	Explanatory Variables	Description and Processing of Data	Data Sources/Data Period	
	VV	Vertically polarized backscatter	ESA Sentinel-1 SAR GRD 1 January 2020~1 January 2021	
	VV Geary's C	Geary's C spatial autocorrelation		
	VH	Horizontally polarized backscatter		
	VH Geary's C	Geary's C spatial autocorrelation		
	VV_Filter	VV with focal median		
	VV_Filter Geary's C	Geary's C spatial autocorrelation		
	VH_Filter	VH with focal median		
	VH_Filter Geary's C	Geary's C spatial autocorrelation		
	DIFF	VV-VH		
	DIFF Geary's C	Geary's C spatial autocorrelation		
Dynamic Factors	RATIO	VH/VV	ESA Sentinel-2 MSI Level-2A 1 January 2015~1 January 2021	
	RATIO Geary's C	Geary's C spatial autocorrelation		
	CRC	(SWIR1-GREEN)/(SWIR1 + GREEN)		
	CRC Geary's C	Geary's C spatial autocorrelation		
	NBR1	(NIR-SWIR1)/(NIR + SWIR1)		
	NBR1 Geary's C	Geary's C spatial autocorrelation		
	NBR2	(NIR-SWIR2)/(NIR + SWIR2)		
	NBR2 Geary's C	Geary's C spatial autocorrelation		
	NDT1	(SWIR1-SWIR2)/(SWIR1 + SWIR2)		
	NDT1 Geary's C	Geary's C spatial autocorrelation		
RDNDVI1	(NIR-RDED1)/(NIR + RDED1)	NASA/USGS Landsat 5/7/8 1 January 1987~1 January 2021		
RDNDVI1 Geary's C	Geary's C spatial autocorrelation			
RDNDVI2	(NIR-RDED2)/(NIR + RDED2)			
RDNDVI2 Geary's C	Geary's C spatial autocorrelation			
NDVI	(NIR-RED)/(NIR + RED)			
NDVI Geary's C	Geary's C spatial autocorrelation			
Landsat percentile	0, 5, 25, 50, 75, 95, 100 percentile indices		NASA/USGS Landsat 5/7/8 1 January 1987~1 January 2021	
Triggering Factors	Precipitation		0, 5, 25, 50, 75, 95, 100 percentile indices	NASA Monthly GPM v6 1 Jun 2000~1 September 2021
	Distance from seismic		Euclidean distance	China Earthquake Networks Center

## Appendix B

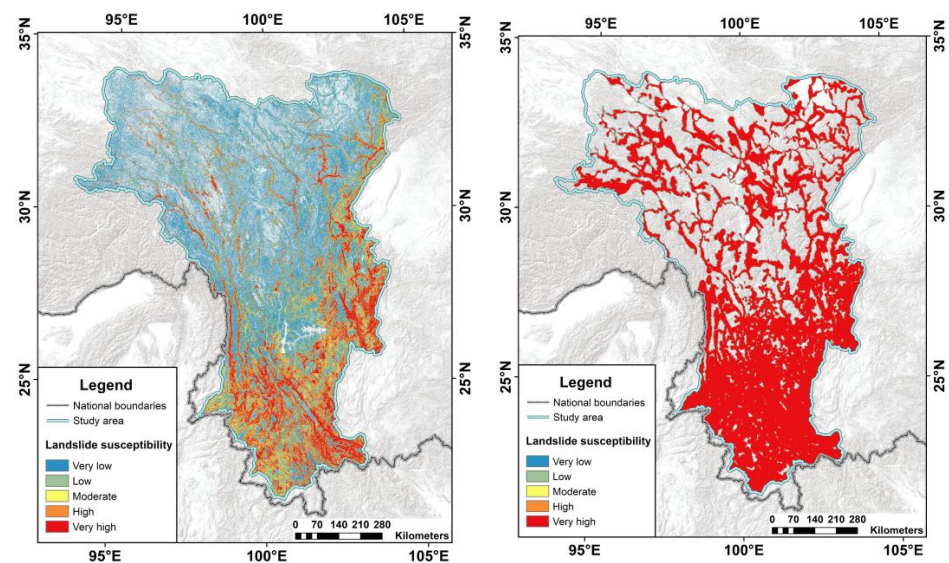


**Figure A1.** Landslide susceptibility mapping using CART and SVM model, respectively. (Left): LS result using CART model. (Right): LS result using SVM model.

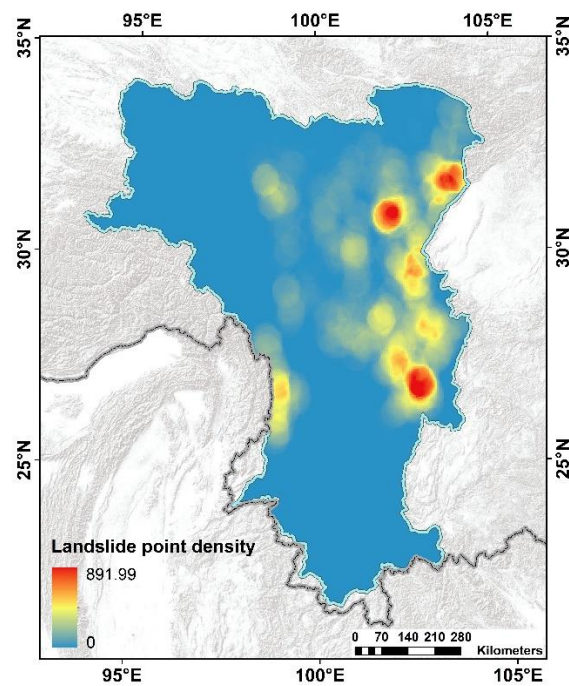


Figure A2. Point density map of training landslide data.

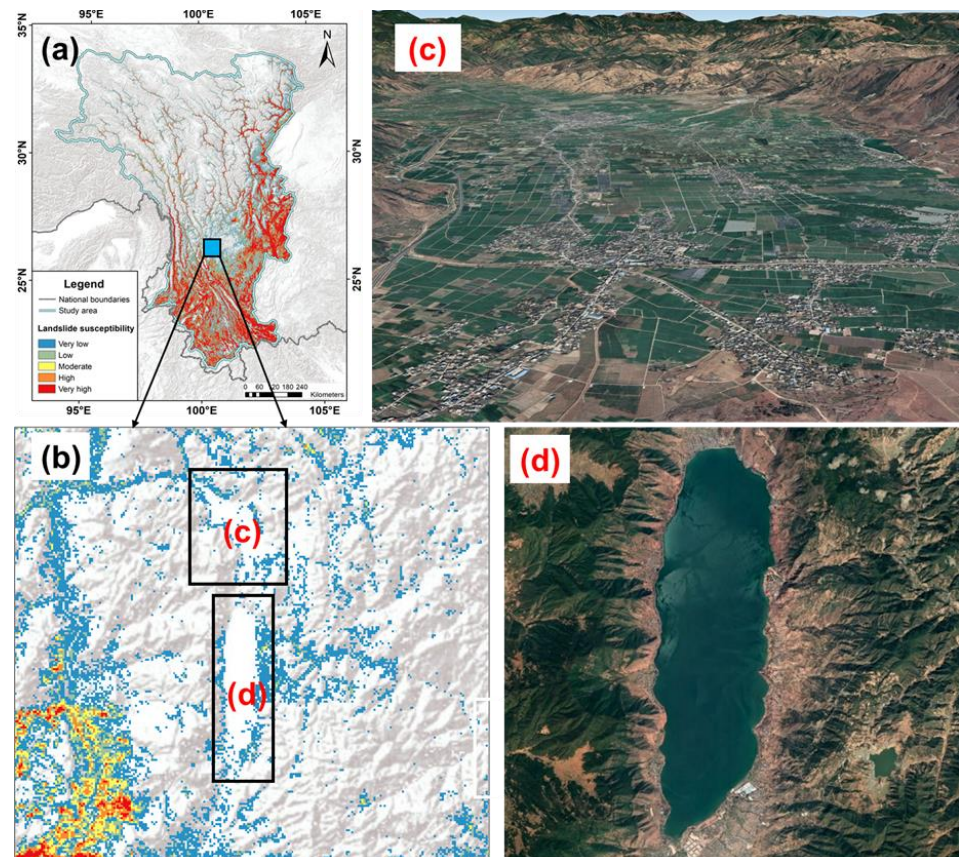


Figure A3. LS values of lake and intermountain plain areas are zero. (a) is the LS map of the Hengduan Mountains region. (c) is a 3D rendering of the plain area from (b), (d) is an aerial view of the lake area from (b).

## References

1. Haque, U.; Blum, P.; da Silva, P.F.; Andersen, P.; Pilz, J.; Chalov, S.R.; Malet, J.-P.; Auflič, M.J.; Andres, N.; Poyiadji, E.; et al. Fatal landslides in Europe. *Landslides* **2016**, *13*, 1545–1554. [[CrossRef](#)]
2. Mizutori, M.; Guha-Sapir, D. *Human Cost of Disasters: An Overview of the Last 20 Years (2000–2019)*; UNDRR/CRED: Leuven, Belgium, 2020; p. 30. Available online: <https://www.undrr.org/publication/human-cost-disasters-overview-last-20-years-2000-2019> (accessed on 1 September 2021).
3. Shugar, D.H.; Jacquemart, M.; Shean, D.; Bhushan, S.; Upadhyay, K.; Sattar, A.; Schwanghart, W.; McBride, S.; de Vries, M.V.W.; Mergili, M.; et al. A massive rock and ice avalanche caused the 2021 disaster at Chamoli, Indian Himalaya. *Science (Am. Assoc. Adv. Sci.)* **2021**, *373*, 300–306. [[CrossRef](#)] [[PubMed](#)]
4. Wang, G.; Zhang, Q.; Yu, H.; Shen, Z.; Sun, P. Double increase in precipitation extremes across China in a 1.5 °C/2.0 °C warmer climate. *Sci. Total Environ.* **2020**, *746*, 140807. [[CrossRef](#)] [[PubMed](#)]
5. Emberson, R.; Kirschbaum, D.; Stanley, T. Global connections between El Nino and landslide impacts. *Nat. Commun.* **2021**, *12*, 2262. [[CrossRef](#)] [[PubMed](#)]
6. Guha-Sapir, D. EM-DAT. Available online: [www.emdat.be](http://www.emdat.be) (accessed on 1 June 2021).
7. Froude, M.J.; Petley, D.N. Global fatal landslide occurrence from 2004 to 2016. *Nat. Hazards Earth Syst. Sci.* **2018**, *18*, 2161–2181. [[CrossRef](#)]
8. Kirschbaum, D.; Stanley, T.; Zhou, Y. Spatial and temporal analysis of a global landslide catalog. *Geomorphology* **2015**, *249*, 4–15. [[CrossRef](#)]
9. Brabb, E.E. Innovative approaches to landslide hazard and risk mapping. In Proceedings of the IVth International Conference and Field Workshop in Landslides, Tokyo, Japan, 23–31 August 1985.
10. Guzzetti, F.; Reichenbach, P.; Cardinali, M.; Galli, M.; Ardiczone, F. Probabilistic landslide hazard assessment at the basin scale. *Geomorphology* **2005**, *72*, 272–299. [[CrossRef](#)]
11. Borrelli, L.; Ciurleo, M.; Gullà, G. Shallow landslide susceptibility assessment in granitic rocks using GIS-based statistical methods: The contribution of the weathering grade map. *Landslides* **2018**, *15*, 1127–1142. [[CrossRef](#)]
12. Ciampalini, A.; Raspini, F.; Lagomarsino, D.; Catani, F.; Casagli, N. Landslide susceptibility map refinement using PSInSAR data. *Remote Sens. Environ.* **2016**, *184*, 302–315. [[CrossRef](#)]
13. Gaidzik, K.; Ramírez-Herrera, M.T. The importance of input data on landslide susceptibility mapping. *Sci. Rep.* **2021**, *11*, 19334. [[CrossRef](#)]
14. Reichenbach, P.; Rossi, M.; Malamud, B.D.; Mihir, M.; Guzzetti, F. A review of statistically-based landslide susceptibility models. *Earth-Sci. Rev.* **2018**, *180*, 60–91. [[CrossRef](#)]
15. Stanley, T.; Kirschbaum, D.B. A heuristic approach to global landslide susceptibility mapping. *Nat. Hazards* **2017**, *87*, 145–164. [[CrossRef](#)]
16. Hong, H.; Tsangaratos, P.; Ilia, I.; Loupasakis, C.; Wang, Y. Introducing a novel multi-layer perceptron network based on stochastic gradient descent optimized by a meta-heuristic algorithm for landslide susceptibility mapping. *Sci. Total Environ.* **2020**, *742*, 140549. [[CrossRef](#)]
17. Castellanos Abella, E.A.; Van Westen, C.J. Qualitative landslide susceptibility assessment by multicriteria analysis: A case study from San Antonio del Sur, Guantánamo, Cuba. *Geomorphology* **2008**, *94*, 453–466. [[CrossRef](#)]
18. Du, G.-l.; Zhang, Y.-s.; Iqbal, J.; Yang, Z.-h.; Yao, X. Landslide susceptibility mapping using an integrated model of information value method and logistic regression in the Bailongjiang watershed, Gansu Province, China. *J. Mt. Sci.* **2017**, *14*, 249–268. [[CrossRef](#)]
19. Kavzoglu, T.; Kutlug Sahin, E.; Colkesen, I. An assessment of multivariate and bivariate approaches in landslide susceptibility mapping: A case study of Duzkoy district. *Nat. Hazards* **2015**, *76*, 471–496. [[CrossRef](#)]
20. Tsangaratos, P.; Ilia, I. Comparison of a logistic regression and Naïve Bayes classifier in landslide susceptibility assessments: The influence of models complexity and training dataset size. *CATENA* **2016**, *145*, 164–179. [[CrossRef](#)]
21. Wang, L.-J.; Guo, M.; Sawada, K.; Lin, J.; Zhang, J. Landslide susceptibility mapping in Mizunami City, Japan: A comparison between logistic regression, bivariate statistical analysis and multivariate adaptive regression spline models. *CATENA* **2015**, *135*, 271–282. [[CrossRef](#)]
22. Chen, W.; Pourghasemi, H.R.; Zhao, Z. A GIS-based comparative study of Dempster-Shafer, logistic regression and artificial neural network models for landslide susceptibility mapping. *Geocarto Int.* **2017**, *32*, 367–385. [[CrossRef](#)]
23. Dou, J.; Yunus, A.P.; Tien Bui, D.; Merghadi, A.; Sahana, M.; Zhu, Z.; Chen, C.-W.; Khosravi, K.; Yang, Y.; Pham, B.T. Assessment of advanced random forest and decision tree algorithms for modeling rainfall-induced landslide susceptibility in the Izu-Oshima Volcanic Island, Japan. *Sci. Total Environ.* **2019**, *662*, 332–346. [[CrossRef](#)]
24. He, Q.; Shahabi, H.; Shirzadi, A.; Li, S.; Chen, W.; Wang, N.; Chai, H.; Bian, H.; Ma, J.; Chen, Y.; et al. Landslide spatial modelling using novel bivariate statistical based Naïve Bayes, RBF Classifier, and RBF Network machine learning algorithms. *Sci. Total Environ.* **2019**, *663*, 1–15. [[CrossRef](#)]
25. Panahi, M.; Gayen, A.; Pourghasemi, H.R.; Rezaie, F.; Lee, S. Spatial prediction of landslide susceptibility using hybrid support vector regression (SVR) and the adaptive neuro-fuzzy inference system (ANFIS) with various metaheuristic algorithms. *Sci. Total Environ.* **2020**, *741*, 139937. [[CrossRef](#)]

26. Vakhshoori, V.; Zare, M. Landslide susceptibility mapping by comparing weight of evidence, fuzzy logic, and frequency ratio methods. *Geomat. Nat. Hazards Risk* **2016**, *7*, 1731–1752. [[CrossRef](#)]
27. Zhu, A.X.; Miao, Y.; Wang, R.; Zhu, T.; Deng, Y.; Liu, J.; Yang, L.; Qin, C.-Z.; Hong, H. A comparative study of an expert knowledge-based model and two data-driven models for landslide susceptibility mapping. *CATENA* **2018**, *166*, 317–327. [[CrossRef](#)]
28. Prakash, N.; Manconi, A.; Loew, S. Mapping landslides on EO data: Performance of deep learning models vs. Traditional machine learning models. *Remote Sens.* **2020**, *12*, 346. [[CrossRef](#)]
29. Huang, F.; Zhang, J.; Zhou, C.; Wang, Y.; Huang, J.; Zhu, L. A deep learning algorithm using a fully connected sparse autoencoder neural network for landslide susceptibility prediction. *Landslides* **2020**, *17*, 217–229. [[CrossRef](#)]
30. Mahalingam, R.; Olsen, M.J. Evaluation of the influence of source and spatial resolution of DEMs on derivative products used in landslide mapping. *Geomat. Nat. Hazards Risk* **2016**, *7*, 1835–1855. [[CrossRef](#)]
31. Mind'je, R.; Li, L.; Nsengiyumva, J.B.; Mupenzi, C.; Nyesheja, E.M.; Kayumba, P.M.; Gasirabo, A.; Hakorimana, E. Landslide susceptibility and influencing factors analysis in Rwanda. *Environ. Dev. Sustain.* **2020**, *22*, 7985–8012. [[CrossRef](#)]
32. Forbes, K.; Broadhead, J. *Forests and Landslides: The Role of Trees and Forests in the Prevention of Landslides and Rehabilitation of Landslide-Affected Areas in Asia*, 2nd ed.; Food and Agriculture Organization of the United Nations: Rome, Italy, 2013.
33. Handwerker, A.L.; Rempel, A.W.; Skarbek, R.M.; Roering, J.J.; Hilley, G.E. Rate-weakening friction characterizes both slow sliding and catastrophic failure of landslides. *Proc. Natl. Acad. Sci. USA* **2016**, *113*, 10281. [[CrossRef](#)]
34. Li, G.K.; Moon, S. Topographic stress control on bedrock landslide size. *Nat. Geosci.* **2021**, *14*, 307–313. [[CrossRef](#)]
35. Yu, X.; Zhang, K.; Song, Y.; Jiang, W.; Zhou, J. Study on landslide susceptibility mapping based on rock–soil characteristic factors. *Sci. Rep.* **2021**, *11*, 15476. [[CrossRef](#)] [[PubMed](#)]
36. Grima, N.; Edwards, D.; Edwards, F.; Petley, D.; Fisher, B. Landslides in the Andes: Forests can provide cost-effective landslide regulation services. *Sci. Total Environ.* **2020**, *745*, 141128. [[CrossRef](#)] [[PubMed](#)]
37. McColl, S.T. Chapter 2—Landslide Causes and Triggers. In *Landslide Hazards, Risks and Disasters*; Shroder, J.F., Davies, T., Eds.; Academic Press: Boston, MA, USA, 2015; pp. 17–42. [[CrossRef](#)]
38. Shahabi, H.; Hashim, M. Landslide susceptibility mapping using GIS-based statistical models and Remote sensing data in tropical environment. *Sci. Rep.* **2015**, *5*, 9899. [[CrossRef](#)] [[PubMed](#)]
39. Hong, Y.; Adler, R.; Huffman, G. Use of satellite remote sensing data in the mapping of global landslide susceptibility. *Nat. Hazards* **2007**, *43*, 245–256. [[CrossRef](#)]
40. Jelének, J.; Kopačková-Strnadová, V. Synergic use of Sentinel-1 and Sentinel-2 data for automatic detection of earthquake-triggered landscape changes: A case study of the 2016 Kaikoura earthquake (Mw 7.8), New Zealand. *Remote Sens. Environ.* **2021**, *265*, 112634. [[CrossRef](#)]
41. Kirschbaum, D.; Stanley, T. Satellite-Based Assessment of Rainfall-Triggered Landslide Hazard for Situational Awareness. *Earth's Future* **2018**, *6*, 505–523. [[CrossRef](#)]
42. Metternicht, G.; Hurni, L.; Gogu, R. Remote sensing of landslides: An analysis of the potential contribution to geo-spatial systems for hazard assessment in mountainous environments. *Remote Sens. Environ.* **2005**, *98*, 284–303. [[CrossRef](#)]
43. Behling, R.; Roessner, S.; Golovko, D.; Kleinschmit, B. Derivation of long-term spatiotemporal landslide activity—A multi-sensor time series approach. *Remote Sens. Environ.* **2016**, *186*, 88–104. [[CrossRef](#)]
44. Mondini, A.C.; Guzzetti, F.; Reichenbach, P.; Rossi, M.; Cardinali, M.; Ardizzone, F. Semi-automatic recognition and mapping of rainfall induced shallow landslides using optical satellite images. *Remote Sens. Environ.* **2011**, *115*, 1743–1757. [[CrossRef](#)]
45. Carlà, T.; Intrieri, E.; Raspini, F.; Bardi, F.; Farina, P.; Ferretti, A.; Colombo, D.; Novali, F.; Casagli, N. Perspectives on the prediction of catastrophic slope failures from satellite InSAR. *Sci. Rep.* **2019**, *9*, 14137. [[CrossRef](#)]
46. Strozzi, T.; Klimeš, J.; Frey, H.; Caduff, R.; Huggel, C.; Wegmüller, U.; Rapre, A.C. Satellite SAR interferometry for the improved assessment of the state of activity of landslides: A case study from the Cordilleras of Peru. *Remote Sens. Environ.* **2018**, *217*, 111–125. [[CrossRef](#)]
47. Zhang, Y.; Meng, X.M.; Dijkstra, T.A.; Jordan, C.J.; Chen, G.; Zeng, R.Q.; Novellino, A. Forecasting the magnitude of potential landslides based on InSAR techniques. *Remote Sens. Environ.* **2020**, *241*, 111738. [[CrossRef](#)]
48. Zhao, C.; Lu, Z.; Zhang, Q.; de la Fuente, J. Large-area landslide detection and monitoring with ALOS/PALSAR imagery data over Northern California and Southern Oregon, USA. *Remote Sens. Environ.* **2012**, *124*, 348–359. [[CrossRef](#)]
49. Bontemps, N.; Lacroix, P.; Larose, E.; Jara, J.; Taïpe, E. Rain and small earthquakes maintain a slow-moving landslide in a persistent critical state. *Nat. Commun.* **2020**, *11*, 780. [[CrossRef](#)]
50. Brunetti, M.T.; Melillo, M.; Peruccacci, S.; Ciabatta, L.; Brocca, L. How far are we from the use of satellite rainfall products in landslide forecasting? *Remote Sens. Environ.* **2018**, *210*, 65–75. [[CrossRef](#)]
51. LaHusen, S.R.; Duvall, A.R.; Booth, A.M.; Grant, A.; Mishkin, B.A.; Montgomery, D.R.; Struble, W.; Roering, J.J.; Wartman, J. Rainfall triggers more deep-seated landslides than Cascadia earthquakes in the Oregon Coast Range, USA. *Sci. Adv.* **2020**, *6*, eaba6790. [[CrossRef](#)]
52. Sharma, A.; Tiwari, K.N. A comparative appraisal of hydrological behavior of SRTM DEM at catchment level. *J. Hydrol.* **2014**, *519*, 1394–1404. [[CrossRef](#)]
53. Arnone, E.; Francipane, A.; Scarbaci, A.; Puglisi, C.; Noto, L.V. Effect of raster resolution and polygon-conversion algorithm on landslide susceptibility mapping. *Environ. Model. Softw.* **2016**, *84*, 467–481. [[CrossRef](#)]

54. Chen, W.; Pourghasemi, H.R.; Panahi, M.; Kornejady, A.; Wang, J.; Xie, X.; Cao, S. Spatial prediction of landslide susceptibility using an adaptive neuro-fuzzy inference system combined with frequency ratio, generalized additive model, and support vector machine techniques. *Geomorphology* **2017**, *297*, 69–85. [[CrossRef](#)]
55. Hong, H.; Ilia, I.; Tsangaratos, P.; Chen, W.; Xu, C. A hybrid fuzzy weight of evidence method in landslide susceptibility analysis on the Wuyuan area, China. *Geomorphology* **2017**, *290*, 1–16. [[CrossRef](#)]
56. Hong, H.; Pourghasemi, H.R.; Pourtaghi, Z.S. Landslide susceptibility assessment in Lianhua County (China): A comparison between a random forest data mining technique and bivariate and multivariate statistical models. *Geomorphology* **2016**, *259*, 105–118. [[CrossRef](#)]
57. Gorelick, N.; Hancher, M.; Dixon, M.; Ilyushchenko, S.; Thau, D.; Moore, R. Google Earth Engine: Planetary-scale geospatial analysis for everyone. *Remote Sens. Environ.* **2017**, *202*, 18–27. [[CrossRef](#)]
58. Jin, Z.; Azzari, G.; You, C.; Di Tommaso, S.; Aston, S.; Burke, M.; Lobell, D.B. Smallholder maize area and yield mapping at national scales with Google Earth Engine. *Remote Sens. Environ.* **2019**, *228*, 115–128. [[CrossRef](#)]
59. Liu, C.; Li, W.; Wu, H.; Lu, P.; Sang, K.; Sun, W.; Chen, W.; Hong, Y.; Li, R. Susceptibility evaluation and mapping of China's landslides based on multi-source data. *Nat. Hazards* **2013**, *69*, 1477–1495. [[CrossRef](#)]
60. Broeckx, J.; Maertens, M.; Isabirye, M.; Vanmaercke, M.; Namazzi, B.; Deckers, J.; Tamale, J.; Jacobs, L.; Thiery, W.; Kervyn, M.; et al. Landslide susceptibility and mobilization rates in the Mount Elgon region, Uganda. *Landslides* **2019**, *16*, 571–584. [[CrossRef](#)]
61. Vodacek, A. A more dynamic understanding of landslide risk. *Nat. Sustain.* **2021**, *4*, 930–931. [[CrossRef](#)]
62. Tao, W.; Huang, G.; Lau, W.K.M.; Dong, D.; Wang, P.; Wen, G. How can CMIP5 AGCMs' resolution influence precipitation in mountain areas: The Hengduan Mountains? *Clim. Dyn.* **2020**, *54*, 159–172. [[CrossRef](#)]
63. Li, W.; Liu, C.; Scaioni, M.; Sun, W.; Chen, Y.; Yao, D.; Chen, S.; Hong, Y.; Zhang, K.; Cheng, G. Spatio-temporal analysis and simulation on shallow rainfall-induced landslides in China using landslide susceptibility dynamics and rainfall I-D thresholds. *Sci. China Earth Sci.* **2017**, *60*, 720–732. [[CrossRef](#)]
64. Bellugi, D.G.; Milledge, D.G.; Cuffey, K.M.; Dietrich, W.E.; Larsen, L.G. Controls on the size distributions of shallow landslides. *Proc. Natl. Acad. Sci. USA* **2021**, *118*, e2021855118. [[CrossRef](#)]
65. Chen, Z.; Song, D.; Dong, L. Characteristics and emergency mitigation of the 2018 Laochang landslide in Tianquan County, Sichuan Province, China. *Sci. Rep.* **2021**, *11*, 1578. [[CrossRef](#)]
66. Dai, F.C.; Lee, C.F. Landslide characteristics and slope instability modeling using GIS, Lantau Island, Hong Kong. *Geomorphology* **2002**, *42*, 213–228. [[CrossRef](#)]
67. Moore, I.D.; Grayson, R.B.; Ladson, A.R. Digital terrain modelling: A review of hydrological, geomorphological, and biological applications. *Hydrol. Processes* **1991**, *5*, 3–30. [[CrossRef](#)]
68. Sidle, R.C.; Ochiai, H. Landslides: Processes, Prediction, and Land Use. *Water Resour. Monogr.* **2006**, *18*, 312. [[CrossRef](#)]
69. Đurić, U.; Marjanović, M.; Radić, Z.; Abolmasov, B. Machine learning based landslide assessment of the Belgrade metropolitan area: Pixel resolution effects and a cross-scaling concept. *Eng. Geol.* **2019**, *256*, 23–38. [[CrossRef](#)]
70. Fabbri, A.G.; Chung, C.-J.F.; Cendrero, A.; Remondo, J. Is Prediction of Future Landslides Possible with a GIS? *Nat. Hazards* **2003**, *30*, 487–503. [[CrossRef](#)]
71. Chang, K.-T.; Merghadi, A.; Yunus, A.P.; Pham, B.T.; Dou, J. Evaluating scale effects of topographic variables in landslide susceptibility models using GIS-based machine learning techniques. *Sci. Rep.* **2019**, *9*, 12296. [[CrossRef](#)]
72. Camilo, D.C.; Lombardo, L.; Mai, P.M.; Dou, J.; Huser, R. Handling high predictor dimensionality in slope-unit-based landslide susceptibility models through LASSO-penalized Generalized Linear Model. *Environ. Model. Softw.* **2017**, *97*, 145–156. [[CrossRef](#)]
73. Pourghasemi, H.R.; Gayen, A.; Panahi, M.; Rezaie, F.; Blaschke, T. Multi-hazard probability assessment and mapping in Iran. *Sci. Total Environ.* **2019**, *692*, 556–571. [[CrossRef](#)]
74. Yalcin, A.; Reis, S.; Aydinoglu, A.C.; Yomralioglu, T. A GIS-based comparative study of frequency ratio, analytical hierarchy process, bivariate statistics and logistics regression methods for landslide susceptibility mapping in Trabzon, NE Turkey. *CATENA* **2011**, *85*, 274–287. [[CrossRef](#)]
75. Zhao, Y.; Huang, Y.; Liu, H.; Wei, Y.; Lin, Q.; Lu, Y. Use of the Normalized Difference Road Landside Index (NDRLI)-based method for the quick delineation of road-induced landslides. *Sci. Rep.* **2018**, *8*, 17815. [[CrossRef](#)]
76. Arnold, D.W.D.; Biggs, J.; Wadge, G.; Mothes, P. Using satellite radar amplitude imaging for monitoring syn-eruptive changes in surface morphology at an ice-capped stratovolcano. *Remote Sens. Environ.* **2018**, *209*, 480–488. [[CrossRef](#)]
77. Leventhal, A.R.; Kotze, G.P. Landslide susceptibility and hazard mapping in Australia for land-use planning—With reference to challenges in metropolitan suburbia. *Eng. Geol.* **2008**, *102*, 238–250. [[CrossRef](#)]
78. Sharma, L.P.; Patel, N.; Debnath, P.; Ghose, M.K. Assessing landslide vulnerability from soil characteristics—a GIS-based analysis. *Arab. J. Geosci.* **2012**, *5*, 789–796. [[CrossRef](#)]
79. Marino, P.; Peres, D.; Cancelliere, A.; Greco, R.; Bogaard, T. Soil moisture information can improve shallow landslide forecasting using the hydrometeorological threshold approach. *Landslides* **2020**, *17*, 2041–2054. [[CrossRef](#)]
80. Akgun, A.; Türk, N. Landslide susceptibility mapping for Ayvalik (Western Turkey) and its vicinity by multicriteria decision analysis. *Environ. Earth Sci.* **2010**, *61*, 595–611. [[CrossRef](#)]
81. Klose, M.; Damm, B.; Gerold, G. Analysis of Landslide Activity and Soil Moisture in Hillslope Sediments Using Landslide Database and Soil Water Balance Model. *Geo-Öko* **2012**, *33*, 204–231.

82. Solikhin, A.; Pinel, V.; Vandemeulebrouck, J.; Thouret, J.-C.; Hendrasto, M. Mapping the 2010 Merapi pyroclastic deposits using dual-polarization Synthetic Aperture Radar (SAR) data. *Remote Sens. Environ.* **2015**, *158*, 180–192. [[CrossRef](#)]
83. Geary, R.C. The Contiguity Ratio and Statistical Mapping. *Inc. Stat.* **1954**, *5*, 115–146. [[CrossRef](#)]
84. Jeffers, J.N.R. A Basic Subroutine for Geary's Contiguity Ratio. *J. R. Stat. Soc. Ser. D Stat.* **1973**, *22*, 299–302. [[CrossRef](#)]
85. Schär, C.; Ban, N.; Fischer, E.M.; Rajczak, J.; Schmidli, J.; Frei, C.; Giorgi, F.; Karl, T.R.; Kendon, E.J.; Tank, A.M.G.K.; et al. Percentile indices for assessing changes in heavy precipitation events. *Clim. Chang.* **2016**, *137*, 201–216. [[CrossRef](#)]
86. Huang, R.; Fan, X. The landslide story. *Nat. Geosci.* **2013**, *6*, 325–326. [[CrossRef](#)]
87. Tien Bui, D.; Tuan, T.A.; Hoang, N.-D.; Thanh, N.Q.; Nguyen, D.B.; Van Liem, N.; Pradhan, B. Spatial prediction of rainfall-induced landslides for the Lao Cai area (Vietnam) using a hybrid intelligent approach of least squares support vector machines inference model and artificial bee colony optimization. *Landslides* **2017**, *14*, 447–458. [[CrossRef](#)]
88. Sales, M.H.R.; Bruin, S.d.; Souza, C.; Herold, M. Land Use and Land Cover Area Estimates From Class Membership Probability of a Random Forest Classification. *IEEE Trans. Geosci. Remote Sens.* **2021**, *60*, 1–11. [[CrossRef](#)]
89. Zhang, L.; Sugathan, P.N. Random Forests with ensemble of feature spaces. *Pattern Recognit.* **2014**, *47*, 3429–3437. [[CrossRef](#)]
90. Felicísimo, Á.M.; Cuartero, A.; Remondo, J.; Quirós, E. Mapping landslide susceptibility with logistic regression, multiple adaptive regression splines, classification and regression trees, and maximum entropy methods: A comparative study. *Landslides* **2013**, *10*, 175–189. [[CrossRef](#)]
91. Erdal, H.I.; Karakurt, O. Advancing monthly streamflow prediction accuracy of CART models using ensemble learning paradigms. *J. Hydrol.* **2013**, *477*, 119–128. [[CrossRef](#)]
92. Pham, B.T.; Prakash, I.; Tien Bui, D. Spatial prediction of landslides using a hybrid machine learning approach based on Random Subspace and Classification and Regression Trees. *Geomorphology* **2018**, *303*, 256–270. [[CrossRef](#)]
93. Youssef, A.M.; Pourghasemi, H.R.; Pourtaghi, Z.S.; Al-Katheeri, M.M. Landslide susceptibility mapping using random forest, boosted regression tree, classification and regression tree, and general linear models and comparison of their performance at Wadi Tayyah Basin, Asir Region, Saudi Arabia. *Landslides* **2016**, *13*, 839–856. [[CrossRef](#)]
94. Huang, Y.; Zhao, L. Review on landslide susceptibility mapping using support vector machines. *CATENA* **2018**, *165*, 520–529. [[CrossRef](#)]
95. Ballabio, C.; Sterlacchini, S. Support Vector Machines for Landslide Susceptibility Mapping: The Staffora River Basin Case Study, Italy. *Math. Geosci.* **2012**, *44*, 47–70. [[CrossRef](#)]
96. Merghadi, A.; Yunus, A.P.; Dou, J.; Whiteley, J.; ThaiPham, B.; Bui, D.T.; Avtar, R.; Abderrahmane, B. Machine learning methods for landslide susceptibility studies: A comparative overview of algorithm performance. *Earth-Sci. Rev.* **2020**, *207*, 103225. [[CrossRef](#)]
97. Gorsevski, P.V.; Gessler, P.E.; Foltz, R.B.; Elliot, W.J. Spatial Prediction of Landslide Hazard Using Logistic Regression and ROC Analysis. *Trans. GIS* **2006**, *10*, 395–415. [[CrossRef](#)]
98. Riegel, R.P.; Alves, D.D.; Schmidt, B.C.; de Oliveira, G.G.; Haetinger, C.; Osório, D.M.M.; Rodrigues, M.A.S.; de Quevedo, D.M. Assessment of susceptibility to landslides through geographic information systems and the logistic regression model. *Nat. Hazards* **2020**, *103*, 497–511. [[CrossRef](#)]
99. Luque, A.; Carrasco, A.; Martín, A.; de las Heras, A. The impact of class imbalance in classification performance metrics based on the binary confusion matrix. *Pattern Recognit.* **2019**, *91*, 216–231. [[CrossRef](#)]
100. Gong, P.; Liu, H.; Zhang, M.; Li, C.; Wang, J.; Huang, H.; Clinton, N.; Ji, L.; Li, W.; Bai, Y.; et al. Stable classification with limited sample: Transferring a 30-m resolution sample set collected in 2015 to mapping 10-m resolution global land cover in 2017. *Sci. Bull.* **2019**, *64*, 370–373. [[CrossRef](#)]
101. Lacroix, P.; Handwerker, A.L.; Bièvre, G. Life and death of slow-moving landslides. *Nat. Rev. Earth Environ.* **2020**, *1*, 404–419. [[CrossRef](#)]
102. Depicker, A.; Jacobs, L.; Mboga, N.; Smets, B.; Van Rompaey, A.; Lennert, M.; Wolff, E.; Kervyn, F.; Michellier, C.; Dewitte, O.; et al. Historical dynamics of landslide risk from population and forest-cover changes in the Kivu Rift. *Nat. Sustain.* **2021**, *4*, 965–974. [[CrossRef](#)]
103. Korup, O.; Seidemann, J.; Mohr, C.H. Increased landslide activity on forested hillslopes following two recent volcanic eruptions in Chile. *Nat. Geosci.* **2019**, *12*, 284–289. [[CrossRef](#)]
104. Lacroix, P.; Dehecq, A.; Taipe, E. Irrigation-triggered landslides in a Peruvian desert caused by modern intensive farming. *Nat. Geosci.* **2020**, *13*, 56–60. [[CrossRef](#)]